



JGR Solid Earth

RESEARCH ARTICLE

10.1029/2019JB019074

Key Points:

- Off-fault plasticity reshapes directivity pulses by reducing peak velocity and increasing dominant period
- Yielding causes peak ground velocity to saturate with respect to increases in both stress drop and epicentral distance
- Off-fault plasticity suppresses the high-frequency fault-parallel pulses that otherwise develop when rupture breaks free surface

Supporting Information:

- Supporting Information S1

Correspondence to:

Y. Wang,
yongfeiw@usc.edu

Citation:

Wang, Y., & Day, S. M. (2020). Effects of off-fault inelasticity on near-fault directivity pulses. *Journal of Geophysical Research: Solid Earth*, 125, e2019JB019074. <https://doi.org/10.1029/2019JB019074>

Received 19 NOV 2019

Accepted 19 MAY 2020

Accepted article online 23 MAY 2020

Effects of Off-Fault Inelasticity on Near-Fault Directivity Pulses

Yongfei Wang^{1,2,3} and Steven M. Day¹

¹Department of Geological Sciences, San Diego State University, San Diego, CA, USA, ²Institute of Geophysics and Planetary Physics, Scripps Institution of Oceanography, University of California, San Diego, La Jolla, CA, USA, ³Now at Southern California Earthquake Center, University of Southern California, Los Angeles, CA, USA

Abstract Near-fault motion is often dominated by long-period, pulse-like particle velocities with fault-normal polarization that, when enhanced by directivity, may strongly excite middle- to high-rise structures. We assess the extent to which plastic yielding may affect amplitude, frequency content, and distance scaling of near-fault directivity pulses. Dynamic simulations of 3-D strike-slip ruptures reveal significant plasticity effects, and these persist when geometrical fault roughness is added. With and without off-fault yielding, these models ($\sim M 7$) predict fault-normal pulse behavior similar to that of observed pulses (periods of 2–5 s, amplitudes increasing with rupture distance until approaching a limit), but yielding systematically reduces pulse amplitude and increases the dominant period. Yielding causes near-fault ($< \sim 2$ km) peak ground velocity (PGV) to saturate with respect to increases in both stress drop and epicentral distance, and, in that distance range, yielding may contribute significantly to the observed magnitude saturation of PGV. The results support the following elements for functional forms in empirical pulse models: (i) a fault-normal distance saturation factor, (ii) a period-dependent and along-strike distance-dependent factor representing directivity, and (iii) an along-strike saturation factor to truncate growth of the directivity factor. In addition to the foregoing effects on long-period fault-normal pulses, the model with off-fault plasticity is very efficient in suppressing the high-frequency fault-parallel acceleration pulses that otherwise develop when rupture breaks free surface. This effect is likely to inhibit the initiation of a sustained supershear rupture triggered by a strong free surface breakage.

1. Introduction

Near-fault ground motions featuring strong pulse-like velocities are of great interest in earthquake seismology and engineering. Pronounced low-frequency, pulse-like fault-normal (FN) ground motions have been widely recorded for earthquakes in strike-slip (e.g., the 1966 Parkfield, the 1971 San Fernando, the 1992 Landers, and the 1994 Northridge earthquakes) and dip-slip (e.g., the 1999 Chi-Chi, the 2009 L'Aquila, and the 2016 Meinong earthquakes) fault systems. The engineering effects of near-fault pulse-like ground motions were strikingly exhibited during the 1994 Northridge earthquake in which great structural damage was attributed to near-fault large, impulsive ground shaking of this type (Finn et al., 1995; Hall et al., 1995; Heaton et al., 1995). Such pulse-like ground motions can have high elastic spectral velocity in (typically) the 2- to 5-s period range, imposing a higher demand on building structures than non-pulse-like motions (Anderson & Bertero, 1987; Bertero et al., 1978; Hall et al., 1995). The ground motion models (GMMs) used to perform probabilistic seismic hazard analysis (PSHA) and inform building codes, if they do not fully consider this near-source effect, may underestimate potential seismic hazards.

The high-intensity, compact waveform, and consequently high damage potential of near-fault pulse-like ground motions is a result of the proximity the recording site to the rupture surface, in combination with directivity effects (e.g., Archuleta & Hartzell, 1981; Day et al., 2008; Heaton, 1982; Somerville et al., 1997; Wald et al., 1996); as a consequence, these motions are frequently referred to as directivity pulses. In this context, directivity (or, more precisely, forward directivity) refers to the amplification of ground motion at sites whose direction from the hypocenter is aligned with (i.e., forms a small angle with) the rupture propagation direction. In this paper, we concentrate on near-fault directivity, namely, the directivity effects occurring within a horizontal distance of the rupture surface that is less than, roughly, the seismogenic depth (~ 20 km). Forward rupture directivity effects occur when (1) the rupture front propagates toward the site and (2) the direction of slip on the fault is consistent with the site direction (Somerville et al., 1997). These

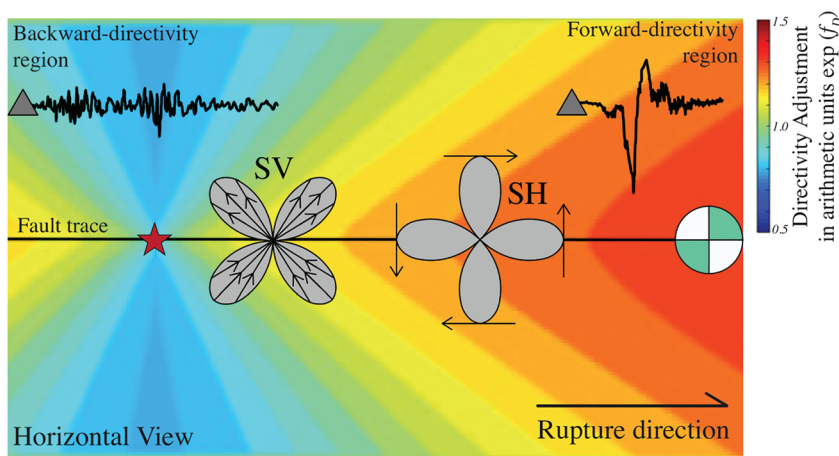


Figure 1. Schematic plan view showing near-fault directivity effects of a vertical right-lateral strike-slip event, modified from Somerville et al. (1997). Representative ground velocities of forward- and backward-directivity sites are extracted from Lucerne and Joshua Tree stations in the 1992 Landers earthquake (source: Somerville et al., 1997). Radiation patterns of SV and SH waves are plotted along the fault trace, respectively. The background colored map is a directivity adjustment in ground motion models (GMMs). This particular directivity correction is based on Bayless and Somerville (2013), which generally illustrates near-fault wedge-shaped amplifications in forward-directivity regions.

two conditions are readily met for the FN ground motion component in strike-slip faulting (Figure 1, based on Figures 2 and 3 of Somerville et al., 1997). As depicted in Figure 1, radiation patterns of SV and SH waves imply that the dominant motion near the fault will be the FN direction as a result of cumulative SH waves ahead of the propagating rupture. On the other hand, even when those conditions are met for a particular earthquake, the characteristic forward directivity effects are not always observed, and, in any case, directivity effects often have diminished strength at frequencies about roughly 0.5 Hz. The latter effect is perhaps owing to three-dimensional heterogeneities and incoherent rupture fronts, as suggested by both theoretical models (e.g., Day et al., 2008; Gritz, 2009) and observational studies (e.g., the frequency-dependent directivity noted by Baltay & Boatwright, 2015, for the unilaterally rupturing 2014 South Napa earthquake). Note also that, for the distance range and frequency band that are considered in the current study, near-field terms in the wavefield cannot generally be neglected nor can source finiteness effects. As a result, directivity effects cannot simply be attributed to a Doppler-like frequency shift (e.g., Douglas et al., 1988). In the near-fault region, especially adjacent to the rupture surface, that simple picture is complicated by near-field and source-finiteness effects.

There have been substantial efforts over the last couple of decades to develop adjustments to empirical GMMs (also known as ground motion prediction equations (GMPEs)) to capture near-fault directivity effects. Adjustment approaches have been based on fitting empirical ground motion data to simple functional forms (e.g., Somerville et al., 1997) and/or theoretical models (e.g., isochrone theory that accounts for the radiation pattern and general behaviors expected for near-fault seismic waves; e.g., Spudich & Chiou, 2008). These directivity adjustments mostly vary with the azimuthal angle and distance of an observing site to the fault, typically predicting (for strike-slip events) amplifications distributed as a wedge centered along the fault trace, as illustrated in Figure 1. Typically, the functional forms in these models include tapers that reduce the predicted directivity effect at smaller magnitude ($M < 6.5$) and larger distance to the fault (>30 km) and sometimes assume that the directivity effect becomes saturated (i.e., becomes insensitive to parameter increases) for rupture distances (toward the site of interest) exceeding some threshold (Abrahamson, 2000; Bozorgnia & Campbell, 2004; Donahue et al., 2019; Somerville et al., 1997). In this paper, we do not focus on gross azimuthal dependence (forward- and backward-directivity), but instead we concentrate on characterizing pulse-like ground motion within the near-fault forward-directivity zone, within a few km of the rupture surface of strike-slip events, using the expressions “directivity pulse” and “near-fault pulse” synonymously. We use numerical simulations to investigate sensitivities of forward directivity (e.g., spatial taper and saturation) to distance to epicenter (recalling that we restrict consideration to rupture-adjacent sites, so this is essentially the same as rupture distance toward the site), predominant

period, and source complexity. The results shed some light on physical mechanisms limiting pulse growth, and may prove useful in adjusting functional forms for the representation of pulse-like near-fault effects in empirical models.

Because of the nonlinearity of structural response to high-amplitude ground pulses, reliable analysis of the performance of a target structure requires characteristic constraints on the pulse waveform, particularly estimates of its amplitude and duration (Hall et al., 1995). The peak ground velocity (PGV; sometimes exceeding 1 m/s) and dominant period of the pulse are important features of high relevance to GMMs and building design codes. A typical range of pulse duration in a magnitude range of Mw 5–8 is 1–10 s (Baker, 2007; Fayjaloun et al., 2017; Shahi & Baker, 2014) and expected value of this duration is also magnitude dependent (Baker, 2007; Shahi & Baker, 2014; Somerville, 2003).

Among factors affecting the amplitude and shape of the pulse-like ground motions are, as stated in Scala et al. (2018), the rupture velocity, hypocentral depth, and the station location relativity to the fault (if in a framework of dipping fault, whether the station is on the hanging wall or on the footwall is also relevant—but our focus will be on vertical strike-slip faults). If the rupture velocity exceeds the shear wave speed (a supershear rupture), the near-fault ground motion changes character. In that case, the low-frequency FN pulse commonly seen in subshear ruptures is substantially reduced in amplitude, and the fault-parallel component becomes dominant (e.g., Aagaard & Heaton, 2004; Bizzarri et al., 2010; Dunham & Bhat, 2008). Thus, the observation of a dominant FN directivity pulse usually implies a rupture velocity below the local shear wave speed. Waveform modeling indicates that pulse duration is influenced by the average slip rise time (Fayjaloun et al., 2017; Scala et al., 2018). Small-scale heterogeneity of coseismic frictional stress affects the amplitude and frequency dependence of pulse-like ground motions by weakening the coherence of the rupture front (e.g., Gallovic, 2016; Gritz, 2009). Moreover, surface ruptures differ from buried ruptures in their excitation of pulse-like ground motions. For example, Somerville (2003) proposes that, while in both cases FN pulses are recognizable, surface-rupturing earthquakes systematically generate weaker near-fault ground motion in a period range of around 0.3–3 s than buried earthquakes. In addition, material heterogeneity tends to reduce the pulse period (Withers, Olsen, Day, & Shi, 2018), and the presence of a low-rigidity shallow layer can change the rupture front shape and thereby affect pulse shapes (Kaneko & Lapusta, 2010).

Off-fault inelasticity (usually in the form of an elastoplastic model) has received considerable attention in model-based studies of rupture, motivated in part by fine-scale geodetic observations of coseismic fault zone deformation (e.g., Brooks et al., 2017; Klinger et al., 2018; Milliner et al., 2016, 2015; Zinke et al., 2014). Plastic yielding during rupture redistributes stresses near the rupture front, in turn affecting the subsequent rupture history and associated ground motion. These effects have been modeled in the framework of continuum plasticity (e.g., 3-D Drucker-Prager [DP], 2-D Mohr-Coulomb, End-cap and Masing type) in recent studies (e.g., Andrews, 2005; Duan & Day, 2008; Dunham et al., 2011a; Hirakawa & Ma, 2016; Roten et al., 2014; Roten, Olsen, Day, & Cui, 2017; Roten et al., 2019; Shi & Day, 2013; Wang et al., 2019; Wollherr et al., 2019, 2018). These models suggest that inelastic deformation can not only reduce peak ground motions (Dunham et al., 2011a; Roten et al., 2012; Roten, Olsen, Day, & Cui, 2017) but also partially filter out high-frequency radiation (Duan & Day, 2008; Ma & Hirakawa, 2013). Moreover, inelasticity may influence the high-frequency attenuation of the acceleration spectra (Shi & Day, 2013). Rupture velocity, to which high-frequency seismic radiation is sensitive (Madariaga, 1977), can also be modified due to off-fault plastic yielding (Andrews, 2005; Duan & Day, 2008), with consequences for the spectral shape of ground motions (Shi & Day, 2013).

In this work, we explore the effects of off-fault inelasticity on the near-fault directivity pulse, with particular attention to effects on pulse amplitude and duration. Initially, we revisit the wavefield components contributing to directivity pulses and review their dependence on rupture velocity and rise time, using simplified 2-D in-plane kinematic ruptures (section 2). Next, we simulate fully dynamic unilateral rupture on a vertical strike-slip fault, considering depth-dependent prestress and rate-and-state friction (section 3). Then, we compare the synthetic near-fault ground motions that travel through elastic and inelastic off-fault media, characterizing the results in terms of near-fault directivity, PGV, and dominant pulse period (section 4). To test the robustness of the inferred effects when some of the model idealizations are relaxed, we also examine simulations that incorporate fault surface roughness (with accompanying heterogeneous prestress) (section 5).

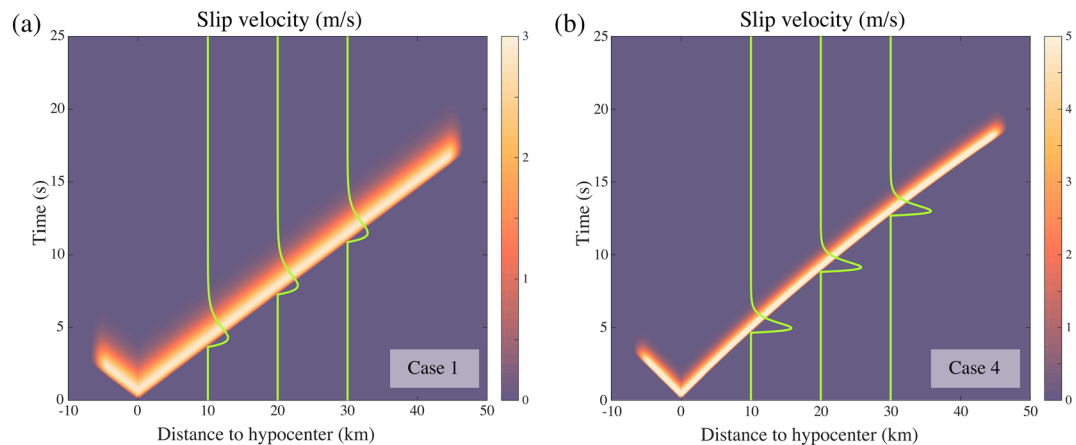


Figure 2. Representative generated spatial-temporal slip velocities (Cases (a) 1 and (b) 4). Green curves show slip velocity time histories at different stations on fault.

2. Two-Dimensional Kinematic Rupture Model

Before we consider fully dynamic unilateral ruptures, we first examine a simplified 2-D in-plane kinematic rupture in an elastic medium. The objective is to review and elucidate the relationship between near-fault directivity pulses and on-fault slip in a simplified context (e.g., neglecting free surface interactions, material nonlinearity, and the complications of dynamic, spontaneously varying rupture velocities, rise times, and slip velocities) supplementing similar kinematic analyses (e.g., Boatwright & Boore, 1975; Boore et al., 1971; Boore & Zoback, 1974; Haskell, 1969). For each subfault element, our slip velocity function is a Brune source time function given by Equation 1:

$$s(t) = \left(\frac{\pi}{\tau}\right)^2 t \exp\left(-\frac{\pi}{\tau}t\right) H(t), \quad (1)$$

where t is time, $H(t)$ is the Heaviside step function and τ controls the rise time of the slip rate function (representative slip velocity functions are illustrated by green solid lines in Figure 2). We generate a kinematic steady-state rupture pulse in which rise time and static slip are constant along the strike except for tapering at the ends of the line fault (to reduce strong stopping phases in near-fault ground motions), as shown in Figure 2. The model parameters and discretization of these 2-D kinematic ruptures (e.g., domain size, bulk properties, and space/time step) are listed in Table S1 in the supporting information. By varying the rupture velocity and rise time, we construct in total five scenarios to illustrate how on-fault rupture behaviors modify the near-fault directivity pulse. For Cases 1 to 3, velocities and rise times are fixed along the strike (Figure 2a), while Cases 4 and 5 have rupture velocities that are linearly increasing and decreasing functions of distance from the hypocenter, respectively (Table S2 and Figure 2b). We numerically solve this problem of 2-D in-plane wave propagation excited by kinematic sources using a generalized finite difference method called support operator with second-order accuracy in time and space. This methodology in terms of its application and verification will be elaborated upon in next section.

As seen in Figure 3a, a representative FN wavefield (generated from Case 1) forms a broad pulse accompanying the rightward propagating rupture. This positive-phase pulse (for the right-lateral slip case) is shown in red, denoting motion directed away from the fault. The pulse is bounded by two negative-phase (blue) regions. The FN ground velocities 3 km from the fault and 40 km along strike from the hypocenter (dark red triangle in Figure 3a) are vertically aligned and plotted in Figure 3b. Beginning with the hypocentral P wave arrival (denoted by a blue dashed line in Figure 3b), the FN components are negative, and grow in amplitude until the arrival of the hypocentral S wave (denoted by a red dashed line). The long-period negative motions between hypocentral P and S waves come from the near- and intermediate-field terms of the P wave (e.g., Aki & Richards, 2002). Similar near- and intermediate-field terms are seen in the TTRH02 record of the 2000 Tottori earthquake (see Figure 6 of Dunham et al., 2011b). The directivity pulses begin with the hypocentral S wave and end with smoothly decaying phases that are associated with arresting of slip on previously ruptured areas (Boore & Zoback, 1974).

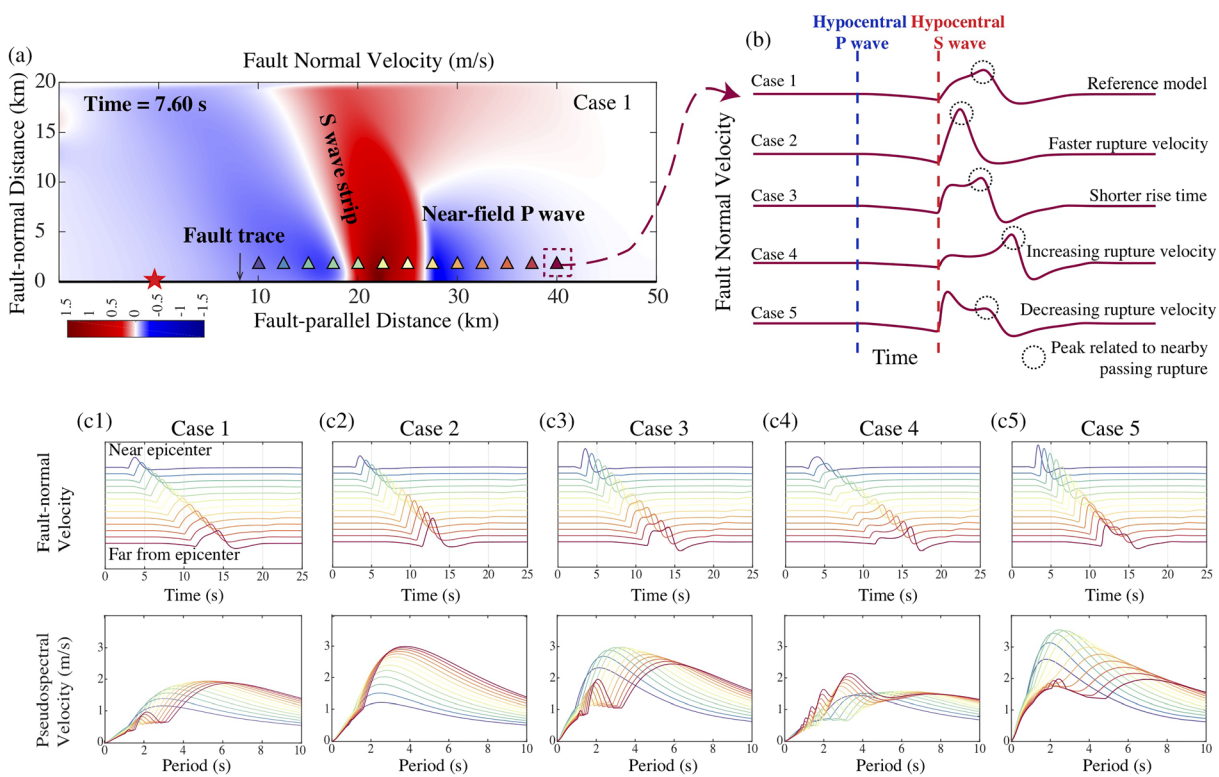


Figure 3. (a) Spatial distribution of 13 stations aligned with the fault trace (black line), superimposed on a wavefield snapshot of fault-normal velocity for Case 1. (b) Fault-normal velocity time histories and c) pseudospectral velocities (PSV) of stations in the five cases described in the text and in Table S1.

The directivity pulse is sensitive to the rupture velocity and rise time (Figure 3b). By comparing the time histories of Case 1 and Case 2, we see that the faster rupture velocity (Case 2) narrows the FN pulse and both amplifies its peak and shifts it to the left (nearer the S arrival time). The shorter rise time in Case 3 leads to near trapezoid-shaped pulse. In Cases 4 and 5, increasing (decreasing) rupture velocity focuses (defocuses) the later peak, because that final peak is associated with very local rupture behavior (e.g., rupture velocity and rise time) as rupture passes by the station. In general, then, the first increment after the hypocentral S wave arrival time results from cumulative S waves arriving from preceding rupture, and the latter part of the pulse is mainly sensitive to the passage of rupture (highlighted by the dashed circles in Figure 3b). In the aforementioned scenarios in which stations are not far from the hypocenter, the total duration of the pulse is related to the overall preceding rupture time. Considering an extreme case (Figure S1) in which a rupture unilaterally propagates along a 200-km-long fault (other parameters remain the same as in Case 1), for a station at large (120 km) along-strike distance (but still adjacent to the rupture), the directivity pulse splits into two pulses: a small one arriving with hypocentral S wave and a later large one related to the passage of rupture. To sum up, in the simplified 2-D cases, within modest along-strike hypocentral distances, rupture acts to form a FN pulse whose amplitude, duration, and shape are cumulatively controlled by the preceding rupture velocity and rise time (and preceding slip distribution, the dependence upon which we neglect for the sake of simplicity in this section).

Figure 3c shows 13 stations at varying hypocentral distance but fixed distance of 3 km from the fault (hypocentral distance is color coded, with purple curves for the station closest to the hypocenter, ranging to red at the largest distance). We compute FN velocities and FN pseudospectral velocities (PSVs) (5% damping). As seen in Figure 3c, durations of directivity pulse and FN PSV of all five models are broadened and intensified over the long-period band (period >8 s) with increasing distance from the hypocenter. This resembles the prediction of directivity effects in GMMs (e.g., Bayless & Somerville, 2013; Chiou & Spudich, 2013; Shahi & Baker, 2013; Spudich & Chiou, 2013) as seen in background color of Figure 1, in which amplification is increased with the epicentral distance at small angles between the receiver direction and the rupture propagation direction.

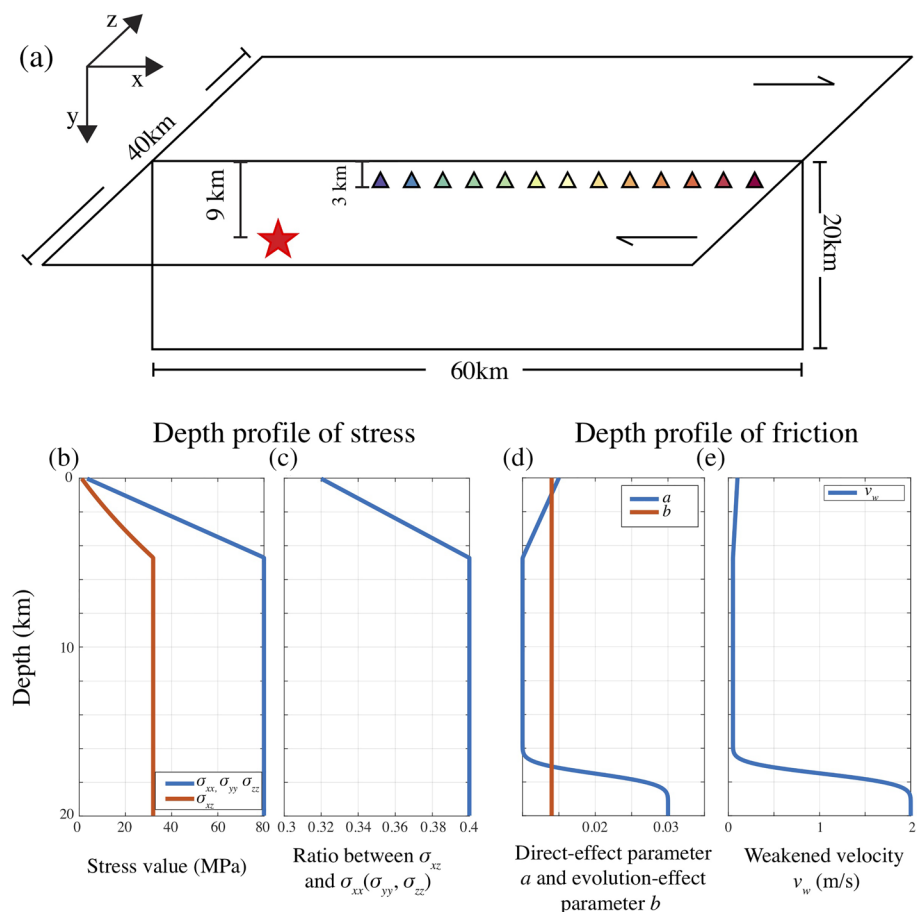


Figure 4. Computational domain size and depth profile of initial stress and friction. These profiles illustrate the parameters labeled as “depth dependent” in Table 1. Colored triangles are locations of ground motion samples used for subsequent analysis.

However, in the intermediate- and high-frequency band, the distance effect departs, to varying degrees, from the simplified, monotonically increasing directivity model. In Case 1 with a constant rupture velocity of 0.8 times the S wave speed, the apparent durations (represented by the period at peak PSV) of FN pulses increase from 2 to 6 s and their peak PSVs vary from about 1 to 2 m/s. However, in that 2- to 6-s period range, the PSV is not necessarily monotonically intensified with distance (purple being the nearest and red the furthest station), as typically assumed in directivity adjustments to GMMs; the Case 1 simulation is only consistent with the latter simplified picture at periods exceeding 6 s, and the amplifications at shorter period are rather complicated. Somerville (2003) introduced the concept of “narrowband directivity,” in which the spectral period of peak directivity amplification scales with earthquake magnitude. As we show in Figure 3, spectral period of peak PSV (at points very near the rupture surface) additionally scales with epicentral distance because the overall duration of a FN pulse is roughly confined by the hypocentral S wave and the rupture passing by the observer. This scaling, even in the very simplified 2-D steady-state slip-pulse scenario, introduces additional complexity in peak PSVs, such that the maximal peak PSV may occur within the span of the rupture rather than at maximal along-fault distance. Indeed, as noted by Spudich et al. (2014), large near-rupture ground motion records such as the Lucerne record of the Landers earthquake are frequently observed within the along-strike end points of the causative rupture trace, even though current directivity amplification adjustment models generally place the amplification maximum at (or just beyond) the rupture ends. Spudich and Chiou (2008) explain this phenomenon using isochrone synthetics, which inherently includes the scaling of peak period with epicentral distance, leading to a complex pattern of peak PSV.

A faster rupture velocity (0.9 S wave speed, close to the terminal velocity of an in-plane rupture), as seen in Case 2, further contracts ground pulses and leads to a narrower range of pulse durations, from 4 to 2 s. In this

Table 1
Model Bulk Properties, Initial Stress Tensor, Frictional Properties, and Nucleation Parameters

Parameter	Symbol	Value
Bulk properties		
<i>P</i> wave speed	α	6,000 m/s
<i>S</i> wave speed	β	3,464 m/s
Density	ρ	2,670 kg/m ³
Viscous damping parameter	γ	4×10^{-4} s
Maxwellian timescale	T_v	0.014 s
Cohesion	c	3 MPa
Internal friction coefficient	$\tan(\phi)$	0.75
Initial stress state		
Initial stress tensor components	σ_{xx}	Depth dependent
	σ_{yy}	Depth dependent
	σ_{zz}	Depth dependent
	σ_{xz}	Depth dependent
Frictional properties		
Direct-effect parameter	a	Depth dependent
Evolution-effect parameter	b	0.014
Reference slip rate	V_0	1 μm/s
Steady-state coefficient at slip rate V_0	f_0	0.6
Evolution distance of state variable	L	0.2
Weakening slip rate	V_w	Depth dependent
Fully weakened friction coefficient	f_w^{ini}	0.3
Initial fault slip rate	V^{ini}	1×10^{-9} m/s
Nucleation parameters		
Nucleation radius	R	3,000 m
Nucleation depth	D	9 km
Overstress	$\Delta\tau^b$	$1 \times \tau^b$

Note. The values of parameters labeled as “depth dependent” can be found in Figure 4. τ^b is a local shear stress at the hypocenter, which is derived from the initial stress tensor.

case, the range of monotonically amplified directivity effects with epicentral distance is extended downward to 2 s, which is consistent with the common observation that directivity is apparent at periods longer than 1 s. While a shorter rise time, as seen in Case 3, does not much vary the range of pulse durations compared to Case 1, the trend of peak PSV from 2 to 6 s becomes complex, with the maximum peak PSV somewhere in the middle-distance range (due to the shorter rise time, the peak PSVs in Case 3 in the range of 2–4 s are intensified compared to those in Case 1). In even more complicated Cases 4 and 5, the long-period directivity effects are observed as expected but the lowest period at which amplification with distance is monotonic goes up to 8 s. In short, in the period band of primary engineering interest (up to, say, ~5 s), the directivity predictions of the simple rupture models are very complex relative to the monotonic distance-amplification at longer period.

In a 3-D strike-slip framework, especially in the presence of a free surface that accommodates surface waves (e.g., Rayleigh waves) and surface-reflected secondary ruptures, the composition of the directivity pulse becomes more complex. Moreover, due to the sensitivity to rupture velocity and rise time illustrated in the foregoing simulations, the directivity pulse is likely to be affected by the spontaneity of the earthquake rupture. In subsequent sections, we will explore how the directivity pulse is shaped by a 3-D spontaneous rupture, emphasizing how the pulse may be further modified by off-fault plastic yielding.

3. Model Setup of 3-D Spontaneous Rupture

Building on understanding gained from the simplified 2-D kinematic rupture models (and previous studies), we model 3-D spontaneous dynamic rupture scenarios on a vertical right-lateral strike-slip fault embedded into elastic and elastoplastic half-space media (Figure 4a). We retain the previous model setups for the dimensions, elastic parameters and discretization (Table S1). Table 1 and Figures 4b–4e describe the elastic/plastic bulk properties, initial stress tensor, and frictional parameters. The parameters of the plasticity model are such that the rupture behaviors, seismic moment, and static stress drop in elastic and elastoplastic scenarios are very similar, simplifying the interpretation of the results.

The off-fault inelasticity follows the DP elastoplastic model (Drucker & Prager, 1952) that contains a pressure-dependent yield surface (without strain hardening or softening, in our application). The DP yield condition (as in, e.g., Shi & Day, 2013) is given by

$$\begin{aligned} \tilde{\tau} &\leq \tau^y \\ \tilde{\tau} &= \sqrt{S_{ij}S_{ij}/2} \\ \tau^y &= c \cos \phi - \sin \phi \sigma_{kk}/3 \end{aligned} \quad (2)$$

where $S_{ij} = \sigma_{ij} - \sigma_{kk}\delta_{ij}/3$ are the deviatoric stress tensor components, $\tilde{\tau}$ is the square root of the second invariant of the deviatoric stress tensor, τ^y is the yield stress, $\sigma_{kk}/3$ is the mean stress, c is the cohesion, and ϕ is the angle of internal friction (values of cohesion and internal friction coefficient ($\tan\phi$) are included in Table 1). We adopt a nonassociative flow rule that brings the stress state smoothly toward the yield surface without volumetric plastic strain involved (no dilatancy). The accumulated plastic strain magnitude η is defined as

$$\begin{aligned} \eta &= \int_0^t \frac{2}{3} d\varepsilon_{ij}^P d\varepsilon_{ij}^P \\ d\varepsilon_{ij}^P &= dS_{ij}/(2\mu) \end{aligned} \quad (3)$$

where $d\varepsilon_{ij}^P$ is the (shear) plastic strain increment and dS_{ij} is the adjustment of deviatoric stress at each time step. Under high strains, the elastoplastic model induces changes in the tangent shear modulus (Erickson

et al., 2017) but does not alter the small-strain elastic moduli, in contrast, for example, to damage mechanics models.

Elastoplastic simulations are subject to contamination by both spurious high-frequency oscillations and inaccuracies due to strain localization. To control these artifacts, as suggested in Duan and Day (2008), we implement two schemes of numerical regularization in our computations: One is to introduce artificial Kelvin-Voigt viscous damping (γ) in the media (Day & Ely, 2002) and the other is to add Maxwellian viscoplasticity that introduces a relaxation time T_v to the adjustment of stress to the yield surface (Andrews, 2005). A value of $0.1\Delta t$ for the viscous damping parameter (Day et al., 2005) and $\Delta x/\beta$ for the characteristic time-scale of the latter viscosity (Andrews, 2005; Duan & Day, 2008) have been found effective in reducing high-frequency noise, and those values are adopted here (Table 1). Other regularization schemes (e.g., Dunham et al., 2011a; Hirakawa & Ma, 2016) have been similarly introduced to effectively stabilize solutions in elastoplastic models.

As seen in Figure 4b, the initial effective normal stress is given by $\bar{\sigma} = 3 + (\rho - \rho_w)g \times \min(Z, Z_0)$ MPa, where Z is a depth. That is, effective normal stress increases with depth at a rate given by the excess of lithostatic pressure over hydrostatic pore pressure, to a depth of Z_0 of 4,700 m, below which it is constant at 80 MPa, reflecting an assumption that fluid overpressure compensates continued lithostatic pressure increase with depth (Rice, 1992). The ratio between shear stress and effective normal stress is illustrated in Figure 4c.

The fault constitutive relation is regularized rate-and-state friction with a strong rate-weakening feature (e.g., Dunham et al., 2011a; Noda et al., 2009; Rojas et al., 2009; Shi & Day, 2013; Wang & Day, 2017). As shown in Figures 4d and 4e, we add a shallow velocity-strengthening ($a - b > 0$) layer with a slightly larger weakened velocity V_w . This feature is important in that its effect is to prevent (or minimize) supershear rupture propagation near the free surface (e.g., Aagaard et al., 2001; Day et al., 2008; Kaneko et al., 2008; Kaneko & Lapusta, 2010), and physically justified, in that the presence of a shallow velocity-strengthening layer has support from laboratory experiments (e.g., Marone, 1998) and observational findings of interseismic shallow creep (e.g., Lindsey et al., 2014), afterslip of large earthquakes (e.g., Marone et al., 1991; Perfettini & Avouac, 2007), and the seismicity deficit (e.g., Shearer et al., 2005).

We numerically solve the 3-D elastoplastic spontaneous rupture propagation problem with the Support Operator Rupture Dynamics (SORD) code (Ely et al., 2008, 2009). This generalized finite difference method has been used in numerous studies of spontaneous dynamic rupture simulation and strong ground motions (Baumann & Dalguer, 2014; Ben-Zion et al., 2012; Ely et al., 2010; Mai et al., 2017; Passone & Mai, 2017; Shi & Day, 2013; Song, 2015; Song et al., 2013; Song & Dalguer, 2017; Vyas et al., 2016; Vyas et al., 2018; Wang et al., 2019; Wang & Day, 2017). The code used here has been verified through tens of elastic and elastoplastic benchmarks in the Southern California Earthquake Center/U.S. Geological Survey (USGS) dynamics earthquake rupture code validation exercise (Harris et al., 2009; Harris et al., 2018). Guided by results in Day et al. (2005), we estimate that the discretization interval employed here (50 m) provides accurate waveform solutions for frequencies up to roughly 7 Hz. The computations were performed on MIRA at the Argonne Leadership Computing Facility (Argonne National Laboratory).

4. Results of a 3-D Spontaneous Dynamic Rupture on a Planar Fault

In this section, we examine some effects of off-fault nonlinearity on the rupture process and near-fault ground motion pulses. The elastic and inelastic cases compared here have very similar seismic moments (7.3×10^{19} Nm (M_w 7.21) and 6.7×10^{19} Nm (M_w 7.19), respectively) and stress drops (5.23 and 5.15 MPa, respectively). Rupture histories are similar in the two cases, except that the plastic case has a somewhat lower overall rupture speed. Figure 5 illustrates a typical example of the contrasting depth profiles (averaged along strike) of coseismic slip with and without off-fault nonlinearity (Figure 5a). There is a systematic decrease in slip for the plastic case in the upper ~3 km, perhaps related to the geodetically observed phenomenon of shallow slip deficit (e.g., Fialko et al., 2005; Simons et al., 2002). Shallow slip in both models is affected by the velocity-strengthening layer that accommodates afterslip or fault creep over an interseismic period (Marone et al., 1991; Rice, 1993), but an extra deficit is accounted for by shallow off-fault inelastic deformation, as also suggested by earlier dynamic rupture propagation models (e.g., Kaneko & Fialko, 2011; Ma, 2008; Roten, Olsen, & Day, 2017).

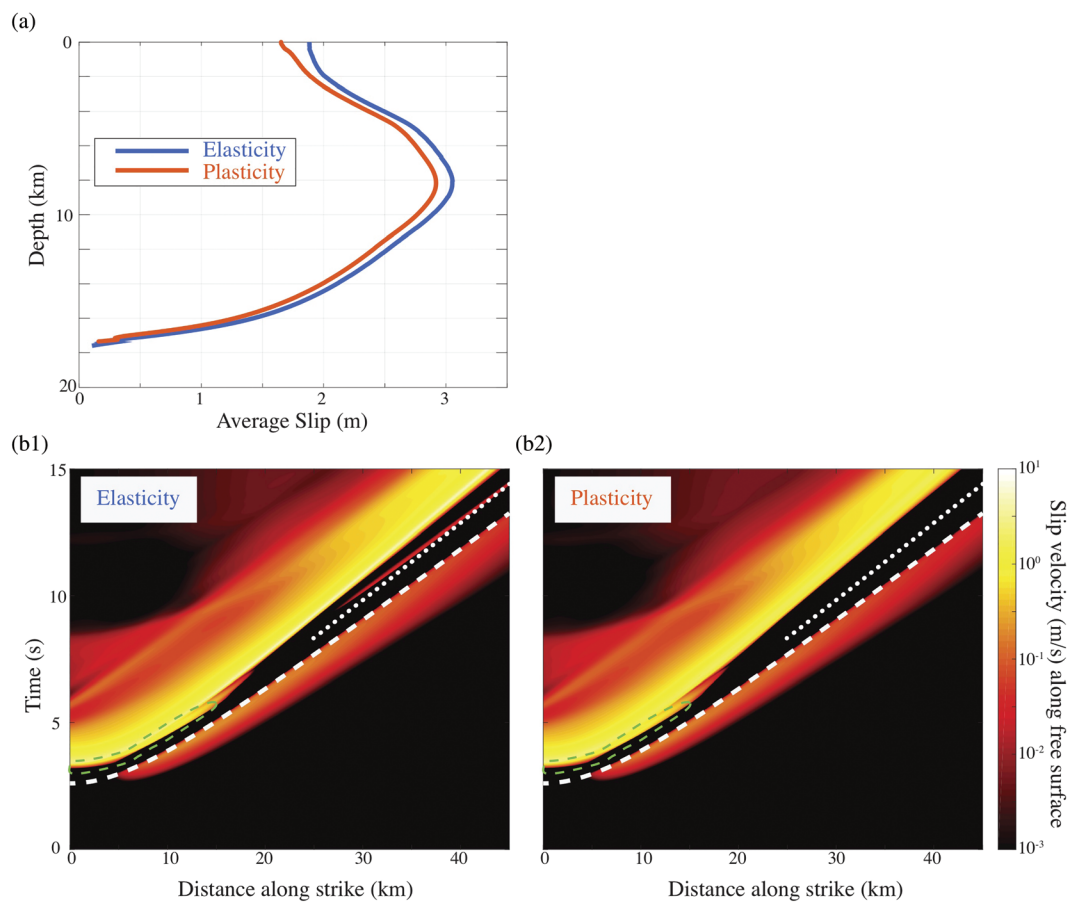


Figure 5. (a) Along-strike averaged slip profiles versus depth and (b) space-time plot of surface slip velocities, in elastic and plastic cases. White dashed lines indicate travel time curves of the hypocentral S wave. White dotted lines indicate Rayleigh wave speed. Green dashed circles enclose surface breakout phases occurring when ruptures break free surface in both elastic and plastic cases.

In Figure 5b, we illustrate rupture behaviors in the form of space-time plots of slip velocity at the free surface. As in Kaneko and Lapusta (2010), there is a weaker slip pulse preceding the main rupture front that becomes recognizable on a logarithmic scale. It is smaller in amplitude (~ 0.1 m/s) than the dominant main rupture front (~ 1 m/s), and it is supershear (i.e., travels faster than the S wave, as indicated by the occurrence of this pulse prior to the white dashed line in Figure 5b). In contrast, velocities of the main rupture fronts in both elastic and plastic cases are slower than the Rayleigh wave speed (white dotted lines), with the plastic case slightly slower than the elastic case (e.g., Andrews, 2005). Moreover, plastic yielding suppresses a very narrow, low-amplitude slip pulse that, in the elastic case, emerges between the initial supershear slip pulse and the main rupture front (thin red streak just above the white dotted line in Figure 5b1). The green dashed lines encircle horizontal apparent supershear rupture episodes associated with surface breakout occurring in both elastic and plastic cases, under certain conditions, which may develop into a persistent supershear rupture front, as in Kaneko and Lapusta (2010).

Figure 5b also shows that the initial supershear pulse heals precisely when the hypocentral S wave arrives. This healing is a result of the “forbidden regime” of rupture velocity, enhanced by stress conditions near the free surface. Steady-state rupture velocity in the range between Rayleigh and shear wave speed is not possible for Mode II cracks (Broberg, 1996, 1999) because in this regime the energy release rate (i.e., the energy flux into the rupture front) is negative (i.e., such a rupture would not absorb elastic strain energy but create it, Das, 2015). There is thus a stress shadow (Figure S2) initiated by the S wave, strengthened and complicated near the free surface (Figure S2d) as similarly seen in Figure 5b of Kaneko and Lapusta (2010). Also

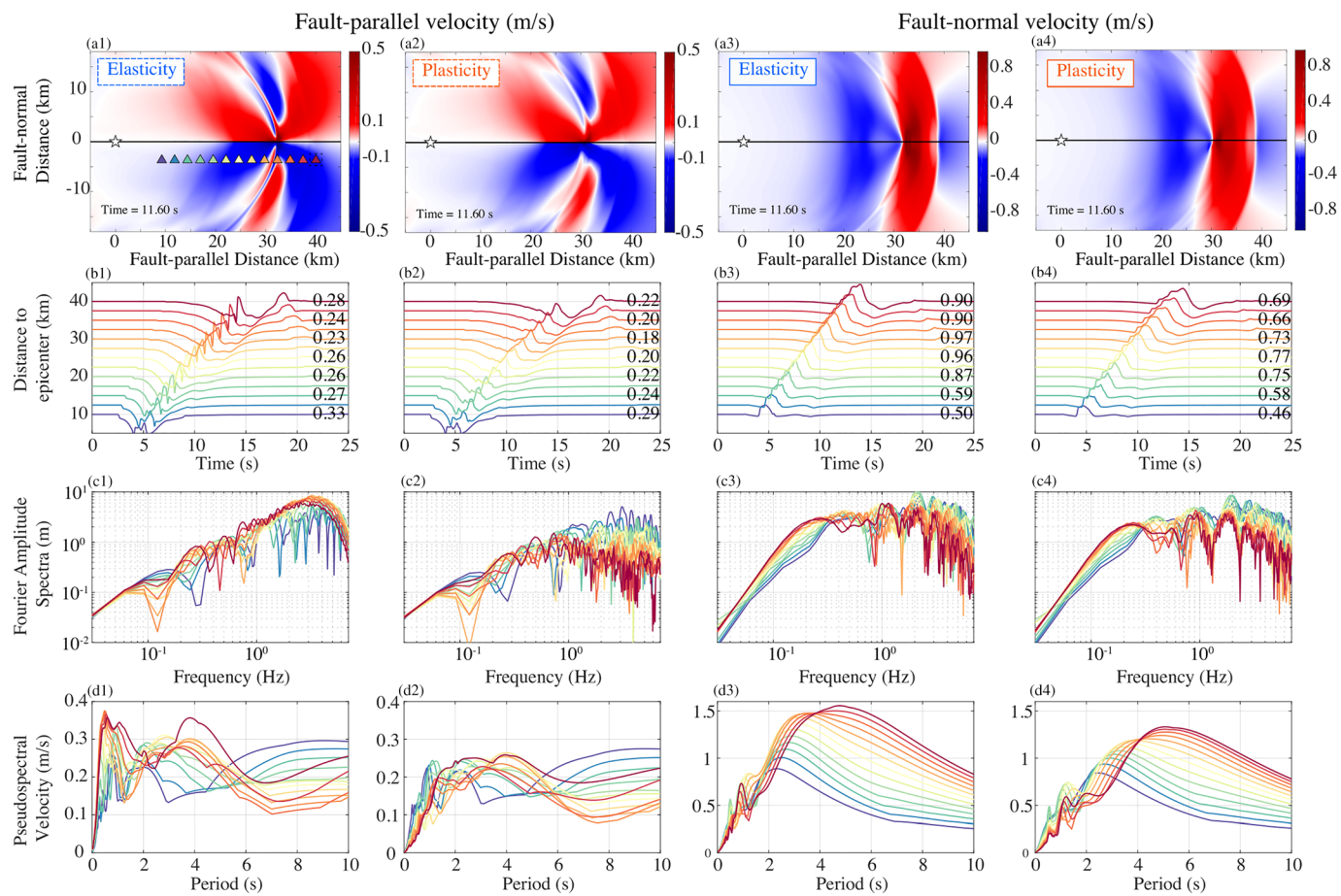


Figure 6. (a) Snapshots of fault-parallel and fault-normal velocities in elastic and plastic cases. A white star locates the epicenter and a black solid line shows the fault trace. The stations are 3 km away from the fault trace. (b) Time series of fault-parallel and fault-normal velocities of stations denoted by colored triangles in Figure 6a1. Numbers on the right side indicate PGV of each trace. (c) Fourier amplitude spectra (FAS) of times series in Figure 6b. (d) Five percent damping pseudospectral velocities (PSVs) corresponding to those time series.

as pointed out in Kaneko and Lapusta (2010), a transition from SV wave to *P* wave boosts the shear stress (Figure S2) leading to a supershear slip pulse (more details are in Text S1 and Figure S2).

Figure 6 compares fault-parallel and FN ground velocities for elastic and plastic cases. A relatively strong FN directivity pulse is present (Figures 6a3, 6a4, 6b3, and 6b4) in both elastic and plastic cases. The directivity pulse is bounded by a preceding near-field *P* wave and a trailing rupture-arrest phase as suggested by the 2-D kinematic simulations in section 3. The shapes of the directivity pulses are very similar in both cases. In Fourier amplitude spectra (FAS) and 5% damping PSV, low frequencies show an enhanced directivity pattern in the form of progressive amplitude increase along the rupture direction (Figures 6c3, 6c4, 6d3, and 6d4). This pattern applies to both elastic and plastic cases and is, again, in qualitative agreement with the 2-D kinematic ruptures. The elastic pulse durations increase with the distance away from the epicenter, in the range of 2 to 5 s (quantified, as before, by the period of maximal PSV). For comparison, an empirical relationship (Baker, 2007; Shahi & Baker, 2014) based on regression analysis predicts a pulse duration of about 5 s for an earthquake with a magnitude of 7.2, consistent with our calculations. Peak PSV at the most distant station in the forward-directivity direction shows a nearly 20% reduction when plastic yielding is introduced (and, in contrast, the peak PSV at the leftmost station is essentially unchanged). That is, the amplification of FN velocity pulses induced by directivity is weakened due to plasticity. This can be understood by reference to the spatial distribution of accumulated plastic strain magnitude (Figure S4), an effect that might also be approximated by introducing a gradually increasing critical slip distance D_c with distance to the epicenter (Andrews, 2005). In addition, the plastic-case pulse widths become wider (Figures 6b4 and 6d4), because

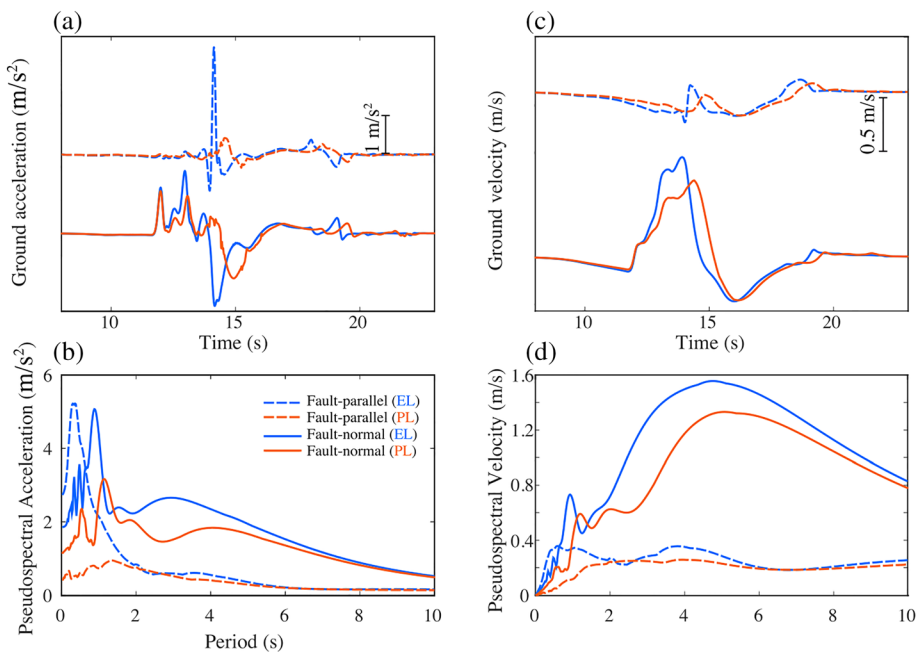


Figure 7. (a) Fault-parallel and fault-normal accelerations at the distant (dark red rightmost triangle in Figure 6a1) station in elastic and plastic cases. (b) Five percent damping pseudospectral acceleration of fault-parallel and fault-normal components in elastic and plastic cases. (c) Fault-parallel and fault-normal velocities and (d) 5% damping pseudospectral velocities in elastic and plastic cases. Solid and dashed lines denote fault-normal and fault-parallel components. Blue and orange colors denote elastic and plastic cases, respectively.

plasticity lowers the overall rupture velocity, to which pulse duration is sensitive (as suggested in 2-D kinematic simulations Case 1 and 2 in section 2), and the tangent modulus acting in incremental deformation is reduced at large strain (Figure 8b and this will be discussed later in this section).

On the other hand, near-fault fault-parallel velocities do not contain low-frequency pulses comparable to those of FN components and show little if any along-strike enhancement. In Figures 6a1 and 6b1 of the elastic case, a strong, high-frequency fault-parallel velocity (a Rayleigh wave) is very clearly seen trailing the rupture front, and we associate this feature with the fact that the upbound rupture front breaks the free surface, resulting in a transient horizontal apparent supershear rupture (indicated by dashed green oval in Figure 5b and see Figure S3). Such high-frequency Rayleigh waves related to the transient apparent supershear near the point where the rupture hits the free surface are similarly reported in other models of predominantly subshear rupture (e.g., Figures 2 and 4 of Bizzarri et al., 2010). Moreover, previous studies have shown that the surface-breaking phase can sometimes induce a sustained supershear rupture (Day et al., 2008; Kaneko et al., 2008). However, in the plastic case, this high-frequency phase is strongly attenuated (Figures 6a2 and 6b2), such that the high-frequency fault-parallel velocity field decays very sharply with a distance from the epicenter, as shown in the FAS plots of Figure 6c2. Plastic response also strongly attenuates fault-parallel short-period PSV (see Figure 6d2, showing ~80% reduction at a period of 0.5 s, relative to elastic case in Figure 6d1). Thus, due to the existence of off-fault plasticity, high-frequency Rayleigh waves induced by surface breakout are subject to very strong absorption by near-fault nonlinearity. This effect may also inhibit the initiation of sustained supershear ruptures triggered by free-surface interaction.

Figure 7 compares ground motions (acceleration and velocity) for the elastic and plastic cases 40 km from the epicenter (rightmost triangle in Figure 6a1), which is the station located in the region of maximum plastic strain. In Figures 7a and 7b, the FN accelerations and velocities (solid curves) in the two cases are very similar in timing of the near-field P wave, hypocentral S wave and S wave radiated during rupture toward the site, reflecting the similarity in rupture histories noted earlier. The large troughs in FN accelerations and peaks of FN velocities (~14 s) show characteristic effects of plasticity, with, in the plastic case, a reduction of peak velocity due to nonlinear deformation of the surrounding medium and an increased pulse width due to an overall slower rupture velocity (Figure 5b) and reduced tangent moduli (Figure 8b) to be discussed

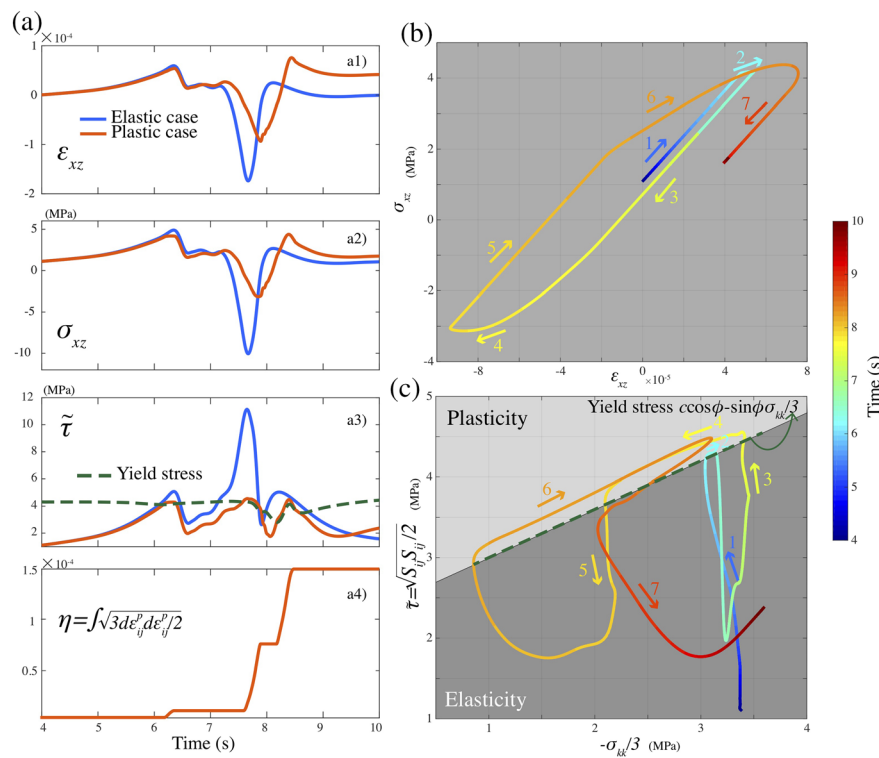


Figure 8. (a) Time histories at a site 5 km from rupture ($z = -5$ km) and 20-km epicentral distance, for both elastic (blue lines) and plastic cases (orange lines). (a1) Shear strain (ε_{xz}), (a2) shear stress (σ_{xz}), (a3) shear stress ($\tilde{\tau}$), and yield stress (τ^y), and (a4) accumulated plastic strain magnitude. (b) Curve of shear stress (σ_{xz}) and shear strain (ε_{xz}) experienced at the site in the plastic case from 4 to 10 s. The seven colored arrows illustrate seven stages discussed in the text, and directions of arrows indicate increasing time. (c) Curve of the stress $\tilde{\tau}$ and the negative value of mean stress ($-\sigma_{kk}/3$) experienced at the site in the plastic case (with the yield stress shown by the green dashed line).

in the next paragraph. The pulse broadening for the plastic case agrees with the behavior suggested by the rupture-velocity dependence in the 2-D kinematic rupture simulations presented earlier. As already noted, off-fault nonlinearity greatly attenuates the high-frequency Rayleigh wave peaks in the fault-parallel acceleration (compare blue and orange dashed curves in Figure 7a), resulting in a FN pseudospectral acceleration (PSA, orange solid line in Figure 7b) that is systematically larger than the fault-parallel PSA (orange dashed line). This predominance of the FN component in the plastic case is consistent with recordings containing directivity pulses (e.g., Day et al., 2008; Somerville et al., 1997). In contrast, the elastic case has larger fault-parallel (blue dashed line) than FN (blue solid line) PSA at a short period, which is disfavored by observations. The PSA and PSV (Figures 7b and 7d) are reduced by the off-fault plasticity over a broad period range.

Figure 8 illustrates the time evolution of stress and strain fields at a site with an epicentral distance of 20 km and a FN distance of -0.5 km (near the light green triangle in Figure 6a1). The shear stress σ_{xz} and shear strain ε_{xz} (see Figure 4a for the definition of coordinate system) are shown for both elastic and plastic cases in Figure 8a1 (strain) and Figure 8a2 (stress), and the comparison illustrates the very significant effects of plastic yielding during the directivity pulse. The plastic case shows reduced amplitudes and delayed peaks in the large-strain regime, relative to those in the elastic case, corresponding to similar effects of plasticity on the velocity pulses (Figure 7c). The curves in Figures 8b and 8c show various stages of the stress strain evolution for the plastic case, as indicated by the reference numbers (Stages 1 through 7), with corresponding times indicated by the changing color of the curves. The curve of the shear stress versus strain, Figure 8b, reveals a hysteresis loop under cycles of loading and unloading at this site. Figure 8c, comparing the square root of the second invariant of deviatoric stress tensor ($\tilde{\tau}$) and yield stress ($cc\cos\phi - \sin\phi\sigma_{kk}/3$), further delineates the elastically and plastically deformed stages. Stage 1 is an initial period of elastic deformation, where

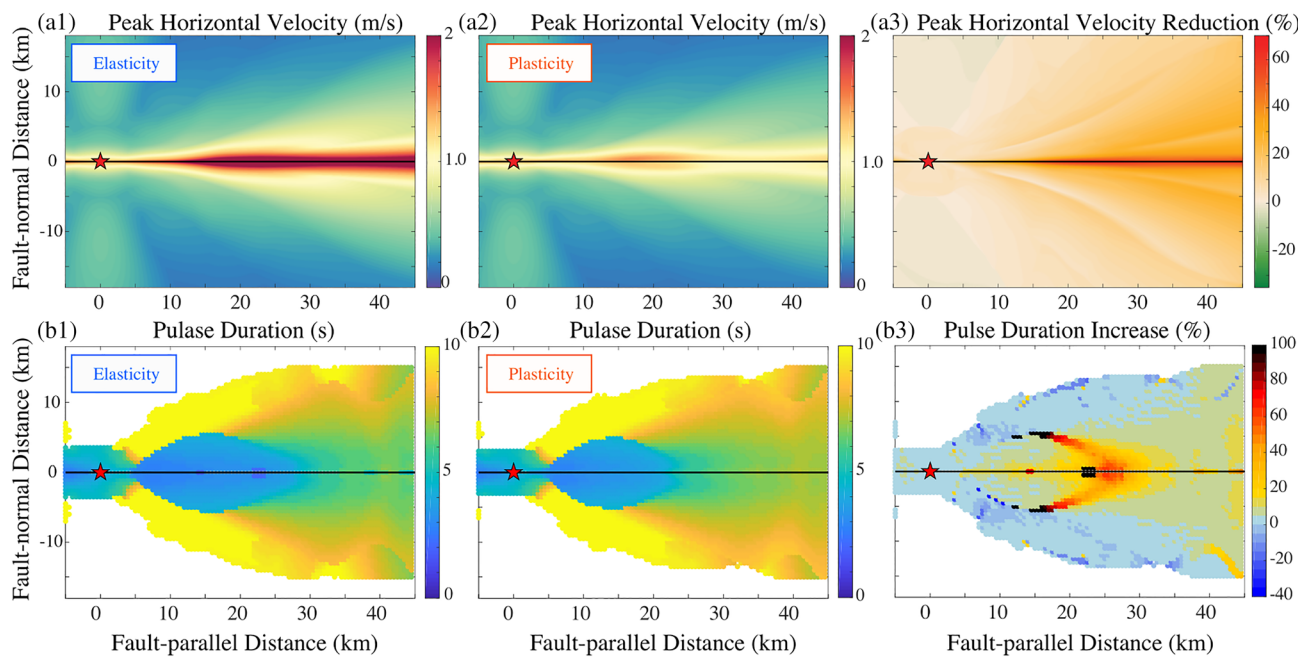


Figure 9. (a) Peak horizontal velocity (PGV) of the (a1) elastic and (a2) plastic cases, and their (a3) difference as a percentage. (b) Pulse duration of the (b1) elastic and (b2) plastic cases and their (b3) difference as a percentage.

stress and strain increments follow the elastic slope (Figure 8b) and deformation state remains below the yield surface (Figure 8c). Stage 2 begins with the onset of plastic deformation at around 6.3 s, where the tangent modulus (stress strain slope) drops to a low value, the stress invariant $\tilde{\tau}$ touches the yield surface (green dashed line in Figures 8a3 and 8c), and plastic strain begins to accumulate (Figure 8a4). Then stress and strain are elastically unloaded and reloaded through Stage 3, with an elastic tangent modulus as in Stage 1, until again entering the plastic regime (Stage 4) of gradually reduced tangent modulus and mounting plastic strain (Figures 8b and 8a4). Stages 5 to 7 alternate between elastic and plastic deformations. In summary, during plastic stages of 2, 4, and 6, the stress $\tilde{\tau}$ exceeds yield stress (Figures 8a3 and 8c), tangent modulus is reduced (Figure 8b), and plastic strain accumulation is rapid near times of 6.3, 7.6, and 8.2 s (Figure 8a4). The tangent moduli during the plastic stages (2, 4, and 6) are variable, reflecting the dependency of the yield surface on mean stress ($-\sigma_{kk}/3$) in our used DP model (see Figure 8c).

Figure 9 shows the spatial pattern of plasticity effects on the FN directivity pulse. Figure 9a illustrates the distribution of peak horizontal velocity (PGV) of the elastic and plastic cases, along with the fractional reduction of PGV due to plasticity. Both cases have spatial distribution of PGV that is roughly wedge-shaped, reflecting forward directivity effects, but in the plastic case PGV is systematically lowered (Figure 9a3). The largest reduction ratios, sometimes exceeding 50%, are concentrated near the fault trace (Roten et al., 2014; Withers, Olsen, Shi, & Day, 2018). We quantify pulse durations, by the method of Shahi and Baker (2014), and these durations are plotted in Figure 9b. The pulse-period predictions resemble those from the simplified equation (in which pulse period scales with along-strike and normal-to-fault distance) proposed by Fayjaloun et al. (2017) (see their Figure 9), which in turn was shown by Fayjaloun et al. (2017) to agree with kinematic rupture simulations. The exceptionally short pulses concentrated from 5 to 20 km away from the epicenter are related to the aforementioned transient supershear associated with free-surface reflection of the main rupture front. The off-fault plasticity extends pulse widths by an average of about 30% near the fault trace, and by up to 100% in a very localized region affected by the high-frequency Rayleigh wave associated with breaking surface. As was the case for amplitudes, the pulse-duration effects of surface breaking high-frequency Rayleigh wave are also much diminished by plastic yielding.

Seismic hazard analyses are typically performed for an orientation-independent measure of horizontal PSA. GMRotD50 introduced by Boore et al. (2006) is a (period-dependent) median value of a set of geometric

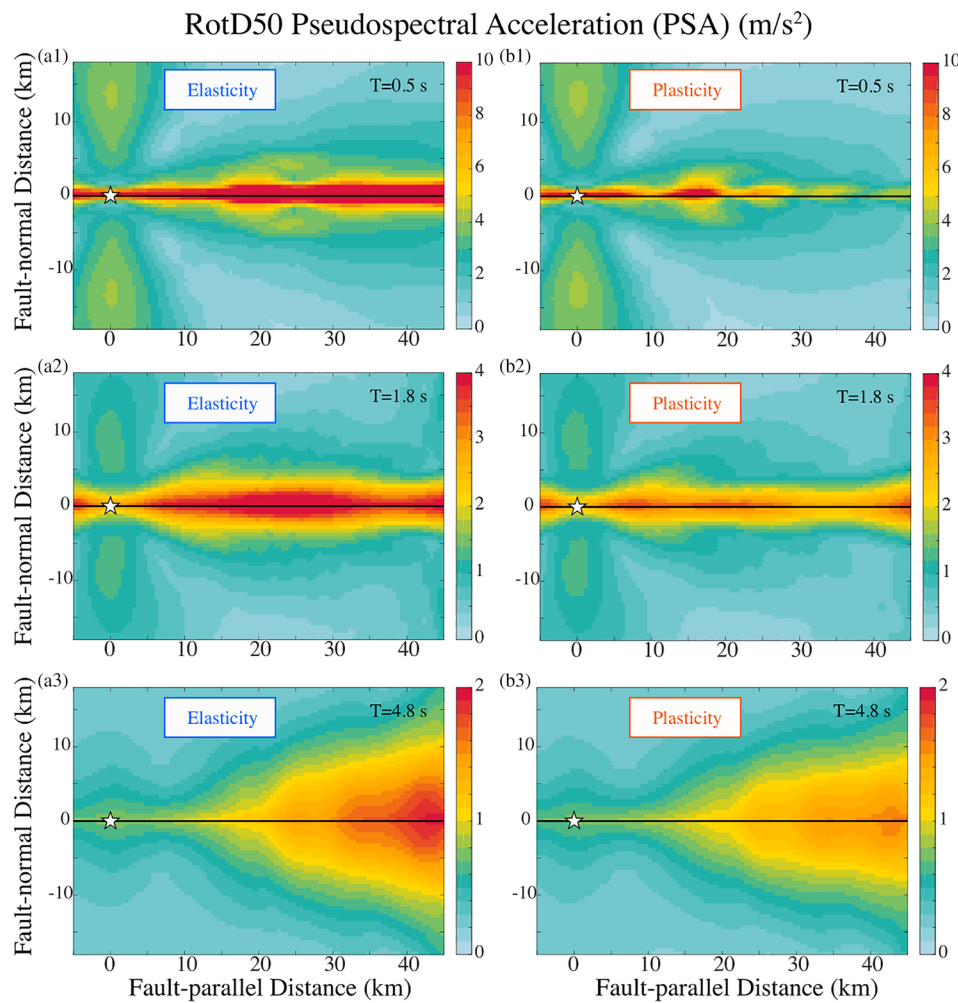


Figure 10. (a) RotD50 maps of 5% damping Pseudospectral acceleration (PSA) at (a1) 0.5 s, (a2) 1.8 s, and (a3) 4.8 s in the elastic case. (b) RotD50 5% damping pseudospectral acceleration (PSA) at (b1) 0.5 s, (b2) 1.8 s and (b3) 4.8 s in the plastic case.

means computed from the as-recorded orthogonal horizontal motions rotated through a set of angles equally spaced on the interval $[0, 90^\circ]$. A new measure RotD50 developed by Boore (2010) preserves orientation independence without computing geometric means and has been adopted in the new GMMs of Enhancement of Next Generation Attenuation Relationships for Western United States (NGA-West2) (Bozorgnia et al., 2014). We therefore examine the effects of off-fault plasticity on this ground-motion measure RotD50 (for periods 0.5, 1.8, and 4.8 s). A principal goal is to provide improved (relative to elastodynamic analyses) guidance for the construction of functional forms for representing the spatial distribution of pulse amplitude and duration. As shown in Figure 10a, in the elastic case, at short and intermediate period, amplification of RotD50 in the forward-directivity region is mainly concentrated along the fault trace, while long-period amplification follows the classic wedge-shaped directivity models (see Figure 1 and Donahue et al., 2019) whereby near-fault amplification increases with epicentral distance (for sites adjacent to the coseismic faulting segment). The simulated amplification in the forward-directivity region supports the feature of the Somerville et al. (1997) empirical model that the directivity slope (rate of amplitude increase with propagation distance toward site) is greater at long period than at short period. In Figure 10b, off-fault plasticity essentially attenuates short- and intermediate-period amplifications of RotD50 concentrated near the fault trace and saturates the long-period amplification, in the sense that it truncates the expansion of the wedge-shaped amplification contours for epicentral distances exceeding 25 km. That saturation effect is consistent with a similar truncation in the empirical directivity model proposed by Abrahamson (2000).

The foregoing results demonstrate that off-fault plasticity can reduce the amplitude and broaden the widths of the directivity pulse, weakening the tendency for amplification to increase with propagation distance in the forward-directivity region (i.e., promoting the along-strike saturation of directivity suggested by, e.g., the model of Abrahamson, 2000). However, interpretation of the effects shown in Figures 9 and 10 is complicated by the fact that yielding affects ground motion directly by limiting shear stress levels at the rupture front and reducing tangent moduli, and indirectly by (usually) reducing the average rupture velocity. To obtain further insight into the effect of plasticity, we isolate the former effect by artificially fixing the rupture velocity through a simplified friction model, but without change to any other model or numerical-implementation parameters (e.g., fault dimension, initial stress, and discretization). The friction adopted here is that employed by Dunham and Bhat (2008). The shear strength, τ_s , weakens linearly with distance within a cohesive zone:

$$\tau_s(x, t) = \max\{\tau_r, \tau_r + A(|x| - v_r t)\}, \quad (4)$$

where τ_r is dynamic friction (equals to $-\mu_r \sigma_n$, dynamic frictional coefficient times normal stress), v_r is the forced rupture velocity (we set 0.9 shear wave speed), A is weakening rate (chosen to ensure at least five mesh points within resulting cohesive zone), x is a spatial distance and t is time. The fault is locked until stress reaches the fault strength (computed by Equation 4) and stress remains constant after fully weakening. By modifying μ_r , we can prescribe the static stress drops (here we neglect overshooting caused by stopping phases). We select three values of stress drop: 1.6, 3.2, and 6.4 MPa and implement them in both elastic and plastic media (Figure 11a). Thus, in total, six cases are simulated and their PGVs along three lines normal to the fault trace (located at 15-, 30-, and 45-km along-strike distance from the epicenter, respectively) are illustrated in Figures 11b1–11b3, on a logarithm scale. As seen in Figure 11b, plasticity induces a saturation of the growth of PGV with respect to FN distance, along-strike distance, and stress drop. Within 1 km of the fault trace, plasticity essentially eliminates the growth of PGV with along-strike distance beyond Line 1 (at 15 km) and greatly reduces its stress drop dependence (PGV is otherwise linearly dependent on stress drop in the elastic case). The maximum near-fault PGV is thereby capped at 2 m/s (reduction by up to a factor of ~3 at some sites, relative to the corresponding elastic model) despite the stress drop and magnitude having been changed from 1.6 MPa and M_w 6.9 to 6.3 MPa and M_w 7.3, respectively.

Empirical data suggest that near-fault PGV saturates as a function of magnitude for large magnitude earthquakes (Boore & Atkinson, 2008) and at present the largest observed PGVs from strike-slip earthquakes are below 2 m/s. Previous suggested explanations are centered on finite fault effects (Baltay & Hanks, 2014; Schmedes & Archuleta, 2008). This is consistent with our models for off-fault distance greater than 1–2 km. However, in our models, plastic yielding appears to impose a stronger limit on PGV at closer distance. Ground motion intensities (e.g., PGV), which are often extrapolated from a farther GMPE due to near-fault sparseness of data, can be overestimated if the near-fault plasticity limit is neglected. Thus, in addition to a finite-fault effect dominating in an intermediate-distance range (1–10 km), inelastic effects (as represented here by plasticity) provide an additional mechanism for the observed magnitude saturation in the near-fault range (~1–2 km). While it is suggestive that the limiting value of 2 m/s seen in Figure 11 roughly coincides with the largest strike-slip PGVs recorded to date, the result is sensitive to our chosen cohesion model and influenced by the absence of complexities in geometry and material properties. For example, Roten, Olsen, Day, and Cui (2017) performed elastoplastic simulations with a range of cohesion and elastic-properties models and found similar near-fault saturation due to plasticity but with occasional exceedances of 2 m/s PGV in some models (albeit only at a small fraction of sites and for magnitude exceeding ~7.5).

Figure 11c shows FN ground velocities recorded at sites 0.5 km from the fault (green triangles in Figure 11b) along three normal-to-fault lines (line styles in Figure 11c are consistent with those in Figure 11b). Plasticity induces larger reductions in pulse amplitudes at sites farther away from the epicenter, and in cases of larger stress drops, in agreement with the saturation effect of PGV discussed earlier. In Figure 11c, we also observe a delay of peak amplitudes, and broadening of pulses (upper row in Figure 11c), for plastic cases relative to elastic cases, just as in the spontaneous rupture scenarios discussed previously. This observation indicates that these effects (amplitude reduction, peak velocity delay, and pulse broadening) can be attributed, at least in part, to reduced tangent moduli due to off-fault plasticity at large strain (around the pulse peak); that is,

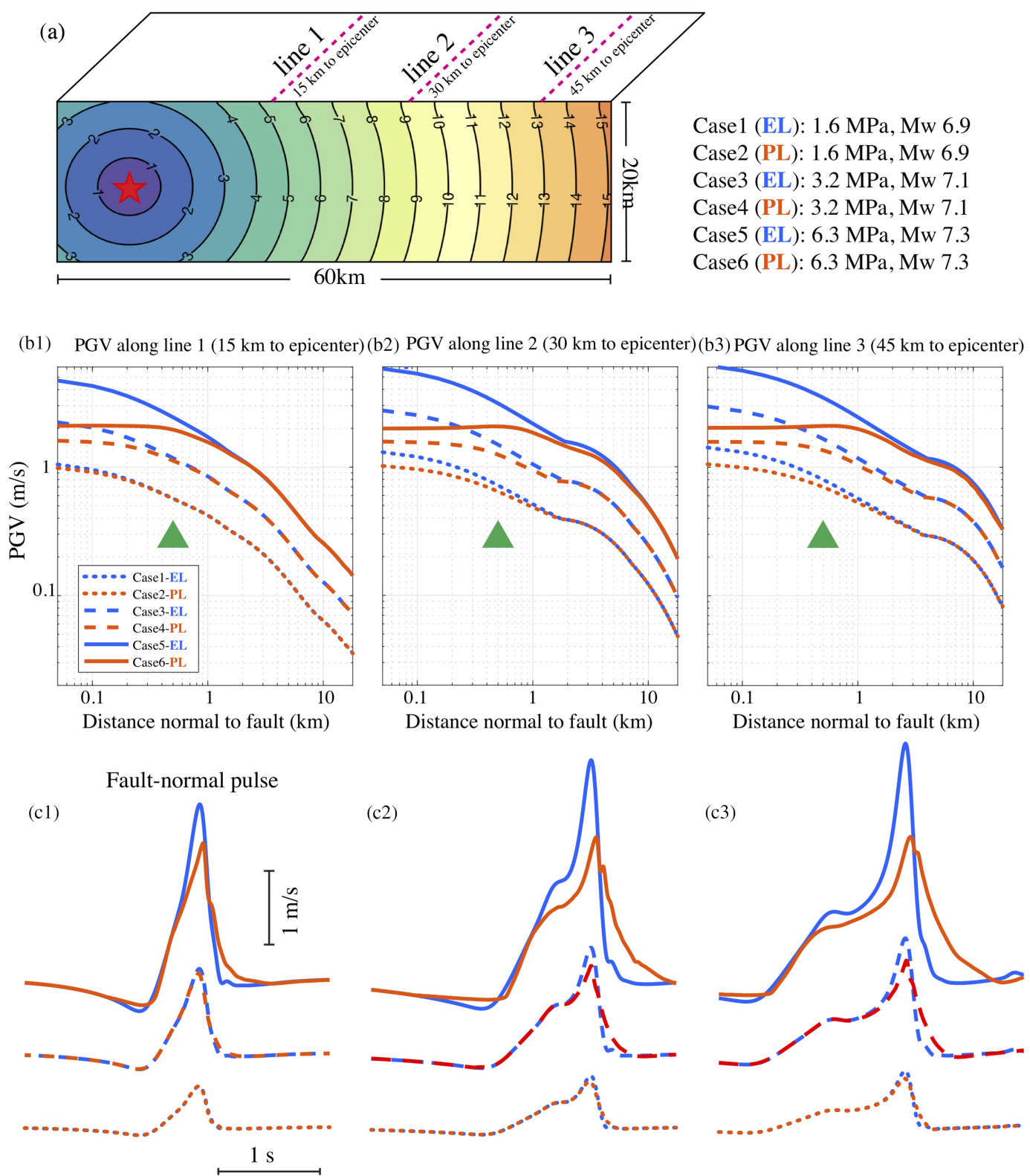


Figure 11. (a) Quasi-dynamic rupture model setup. Rupture front time contours are plotted on the fault plane, showing the prescribed constant rupture velocity (90% shear wave speed). Six elastic and plastic cases are simulated, with three prescribed stress drops. Resultant magnitudes are labeled. (b) Peak horizontal velocity (PGV) along the normal-to-fault lines at along-strike distances of (b1) 15 km, (b2) 30 km, and (b3) 45 km from the epicenter. (c) FN velocity pulses at the station of 0.5 km from the fault (indicated by green triangles in b) along the normal-to-fault lines (c1, c2, and c3 correspond to Line 1, Line 2, and Line 3, respectively) shown in (a) and (b). Line styles corresponding to different cases are consistent with those in (b).

those effects (in the spontaneous-rupture case) are not simply a reflection of rupture velocity reductions due to plastic yielding.

5. Results of a 3-D Spontaneous Dynamic Rupture on a Rough Fault

The foregoing models are smooth, both in the geometry of the fault surface and the propagation of rupture. Since near-field pulses reflect interference of arrivals associated with rupture finiteness, it is appropriate to investigate the extent to which the effects of plasticity noted in the previous section persist when these simplifications are relaxed. In this section, we do so by introducing a rough fault surface. Natural faults manifest varying degrees of geometrical complexities spanning from large-scale branching and segmentation (e.g., Ben-Zion & Sammis, 2003) to small-scale variations on the fault surface (e.g., Candela et al., 2009; Power & Tullis, 1991; Renard et al., 2006; Sagy & Brodsky, 2009). Recent theoretical studies show that geometrical variations of the fault surface lead to ensembles of complex rupture with varying directionalities and magnitudes (e.g., Fang & Dunham, 2013), modifying the radiated seismic spectrum and radiation pattern. In particular, those complexities boost high-frequency ground motions (Dunham et al., 2011b), bringing them into general accord with the aggregated statistics of recorded motions, as reflected in GMPEs (e.g., Kieler et al., 2014; Shi & Day, 2013; Withers, Olsen, Day, & Shi, 2018). The previous rough fault modeling studies have not focused on the dynamics of low-frequency pulses, nor on the degree to which those pulses are sensitive to off-fault plasticity.

We specify fault roughness using an approach closely following Shi and Day (2013). The fault roughness model (Figure S5a) follows a self-similar (Hurst Exponent 1) fractal distribution up to a wavelength cutoff of 200 m. The distribution of deflection distances from a plane is generated in the wavenumber domain (as in Andrews & Barall, 2011) and, after transformation to the spatial domain, the amplitudes of the perturbations are scaled by a specified amplitude-to-wavelength ratio α defined as $\alpha = h_{rms}/L$, where L is the total length of the fault in the along-strike direction and h_{rms} is the root-mean-square roughness of the 2-D perturbation profile (more details to see Appendix A of Shi & Day, 2013). Power and Tullis (1991) estimate α to be in a range from 10^{-3} to 10^{-2} for natural faults. We select an intermediate roughness, $\alpha = 10^{-2.3} \approx 0.005$ in subsequent analysis. Apart from fault geometry, we keep the rest of the model inputs (including elastic and plastic parameters) identical to those of the planar fault scenario of the last section. Comparison of the elastic and plastic cases is facilitated by the similarity of the resultant seismic moments and stress drops in the two cases: moments of 5.0×10^{19} Nm (Mw 7.10) and 4.5×10^{19} Nm (Mw 7.1), respectively, and static stress drops of 5.33 and 5.32 MPa, respectively (see also Figure S6, comparing average static slip and ground surface slip velocity). Comparison of Figure S6 with Figure 5 for the planar fault scenario shows some of the complexities introduced by fault roughness, including transient supershear ruptures between the first supershear pulse and the main, sub-Rayleigh rupture front (especially between about 20 to 40 km along-strike distance). The off-fault plasticity leads to (1) smaller average slip at shallow depth (Figure S6a) and (2) a weakened SV-to-P conversion (Figure S6b2), both of which are consistent with the plasticity effects in the planar-fault scenario.

In Text S2, we provide details of plastic-yielding effects on ground velocities in the rough-fault simulations. We summarize those results (this paragraph) and elaborate on some period-dependent effects (next paragraph). While fault-parallel and FN ground velocities are more complex (e.g., contain more high-frequency arrivals) than in the planar-fault case, the FN pulses have very similar character, retain similar spectral characteristics in long-period band, and pulse duration still scales with epicentral distance. The effects of plasticity damp the high-frequency Rayleigh and S waves associated with supershear transients, broaden the directivity pulse widths, and reduce directivity-enhanced amplifications (more details in Text S2), in a manner similar to that seen in planar-fault study. The rough fault case contrasts with the planar fault case in that the FN spectra display a second characteristic timescale, apparently associated with passage of the rupture front (note, e.g., the secondary pulses starting at around 13 and 15 s in Figure S7b and the discussion in Text S2). The general wedge shape of near-fault PGV contours, reflecting directivity effects, occurs in both elastic and plastic cases and has superimposed upon it multiple localized concentrations of PGV that are correlated to the fault geometry (Figure S8).

Figure 12 shows the spatial distribution of RotD50 (for periods 0.5, 1.8, and 4.8 s). In both elastic and plastic cases, high values of RotD50 are concentrated near the fault in the short- and intermediate-period bands

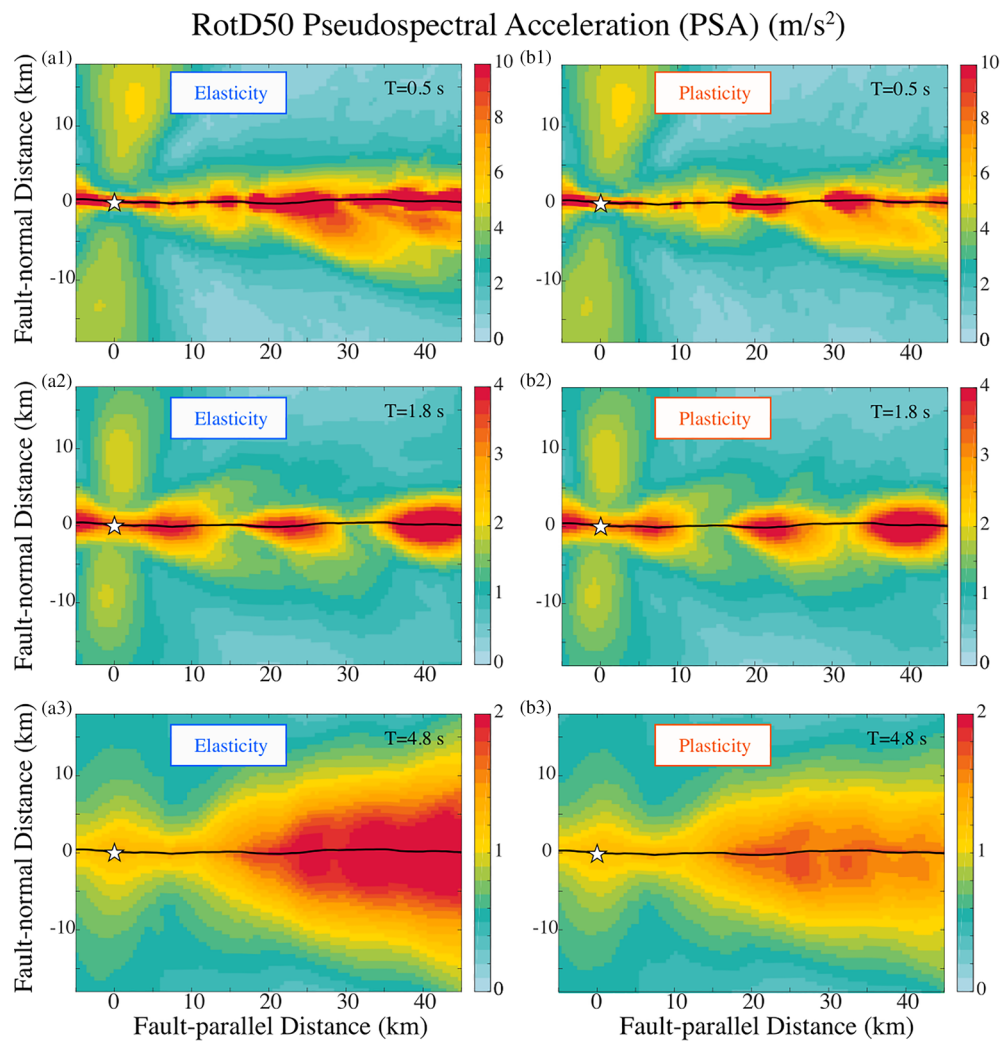


Figure 12. (a) RotD50 maps of 5% damping pseudospectral acceleration at (a1) 0.5 s, (a2) 1.8 s, and (a3) 4.8 s near a rough fault in the elastic case. (b) RotD50 5% damping pseudospectral acceleration at (b1) 0.5 s, (b2) 1.8 s, and (b3) 4.8 s near a rough fault in the plastic case.

(Figures 12a1, 12a2, 12b1, and 12b2). Roughness adds fluctuations to the relatively simple distribution of RotD50 seen in the planar fault case (Figure 10). Off-fault plasticity effects are period dependent. Plasticity attenuates short-period amplification of RotD50 and constrains the directivity-induced short-period amplification area to a zone very close to the fault trace while only minimally impacting the spatial pattern of intermediate-period RotD50. Long-period RotD50 largely reflects the amplitude and period of the FN pulse and is strongly affected by plasticity. In the elastic case, directivity induces a wedge-shaped forward-directivity region (Figure 12a3) within which the near-fault RotD50 increases with epicentral distance for rupture-adjacent sites (i.e., those between the rupture endpoints). This behavior is very similar to that of the planar fault case (Figure 10). For the plastic case (Figure 12b3), in contrast, the along-strike increase of the long-period RotD50 ceases at distance of about 25 km from the epicenter. If we measure a FN width by the FN distance to a given (say 1.2 m/s^2) RotD50 contour, for example, that reaches a maximum of roughly 8 km at 25 km from the epicenter, after which it remains essentially constant, as seen in Figure 12b3. In summary, losses from plasticity both diminish the overall intensity of the directivity-induced amplification wedge and cause the effect to saturate, that is, truncate its growth along strike and in the FN direction. In this respect, our simulations with plasticity favor empirical models for near-fault directivity (GMPE directivity factors) that include a distance saturation effect

(Abrahamson, 2000), and the simulations may also provide guidance for improving distance tapers used in those models, which are otherwise relatively poorly constrained.

6. Discussion

The simulations in section 4 delineate effects of off-fault plasticity on directivity-enhanced FN ground motion pulses (their spatial variations, time domain features, and spectral characteristics). The simulations in section 5 indicate that the main effects do not appear to be highly sensitive to the geometrical simplifications of the model, in that results from the simplified planar fault model carry over to models with fractal roughness. In this section, we further explore the limits of applicability of the results by considering their sensitivity to a change in the dynamics of rupture from a crack-like mode to a self-healing pulse-like mode. Then we discuss the implications of our results for empirical directivity-pulse models, including the way in which their distance and magnitude dependencies are formulated. Finally, we discuss some limitations of the study imposed by model simplifications and unexplored parameter ranges.

6.1. Directivity Pulse in Self-Healing Rupture

So-called pulse-like rupture denotes a mode of rupture characterized by a slip-velocity rise time much shorter than the total duration of the rupture process (note that this use of the term “pulse” is distinct from its use to describe the ground motion waveforms). The pulse-like rupture has been broadly recognized in many seismological, analytical, computational, and experimental studies (e.g., Heaton, 1990; Lu et al., 2010; Melgar & Hayes, 2017; Nielsen & Madariaga, 2003; Zheng & Rice, 1998). Numerous mechanisms have been hypothesized to account for pulse-like rupture, including dynamic (velocity) weakening friction such as that expected from flash heating (e.g., Goldsby & Tullis, 2011) and thermal pressurization (e.g., Noda et al., 2009) mechanisms, heterogeneity of fault strength/stress (e.g., Beroza & Mikumo, 1996), fault zone compliance (e.g., Huang & Ampuero, 2011), and minimum rupture dimension (e.g., Day, 1982). These can roughly be classed as local effects, which we term self-healing (slip duration at a point controlled by local frictional resistance), and nonlocal wave-mediated interactions (slip duration controlled by wave-induced perturbations to the stress field), which we term geometrical. These would by no means be expected to operate independently, but one class may dominate if it has a characteristic time much shorter than the other. For example, Wang et al. (2019) show that the rupture pulse duration in the 2015 Nepal Gorkha earthquake is strongly associated with the geometry of a geologically plausible model of the Main Himalayan Thrust, on the basis of dynamic rupture modeling that matches the near-field high-rate GPS recording directly (15 km) above the fault. Similarly, the spontaneous rupture models in sections 4 and 5, although they can support a self-healing behavior, all were set up with parameter choices such that slip duration was principally controlled by down-dip fault width (and to some extent by fault roughness effects, in the case of section 5), that is, they are geometrically controlled. In contrast, Aagaard and Heaton (2008) show that self-healing dominated rupture can potentially compact the directivity-induced FN ground-velocity pulse. We therefore supplement the results of sections 4 and 5 by considering self-healing rupture in order to further assess how plasticity affects directivity-induced ground motion pulses.

As noted by Wang and Day (2017), a transition to self-healing dominated rupture can be achieved by tuning the weakening slip rate V_w so as to vary the critical stress level τ_{pulse} defined in Zheng and Rice (1998). We retain all the model setups of the planar fault scenarios but use a higher weakening slip rate (0.1 m/s) than that adopted in preceding sections (0.05 m/s in Table 1), so that the average rise time (measured by the period when slip velocity exceeds 0.01 m/s) now is systematically decreased, from about 3 s in the previous cases to 1 s (Figure S9), giving self-healing ruptures in both elastic and plastic cases. Resultant seismic moments of elastic and plastic cases are 4.6×10^{19} Nm (M_w 7.08) and 4.0×10^{19} Nm (M_w 7.03), respectively. The static stress drops of elastic and plastic cases are 3.98 and 3.84 MPa, respectively.

We perform an analysis of ground motions along the same fault-parallel station line as in section 4. Results in Figure 13 (using the same color convention as in Figure 6 to associate stations with spectral plots) are qualitatively very similar to those seen for the longer rise time cases in sections 4 and 5. The prominence of the FN directivity-induced pulse, the dominance of FN PSV relative to the fault-parallel component, and the increase of FN pulse duration with along-strike distance resemble the earlier results, in both elastic and plastic cases. There are some quantitative differences due to the smaller rise time in the self-healing model. In the elastic case, results are in good agreement with expectations from the work of Aagaard and

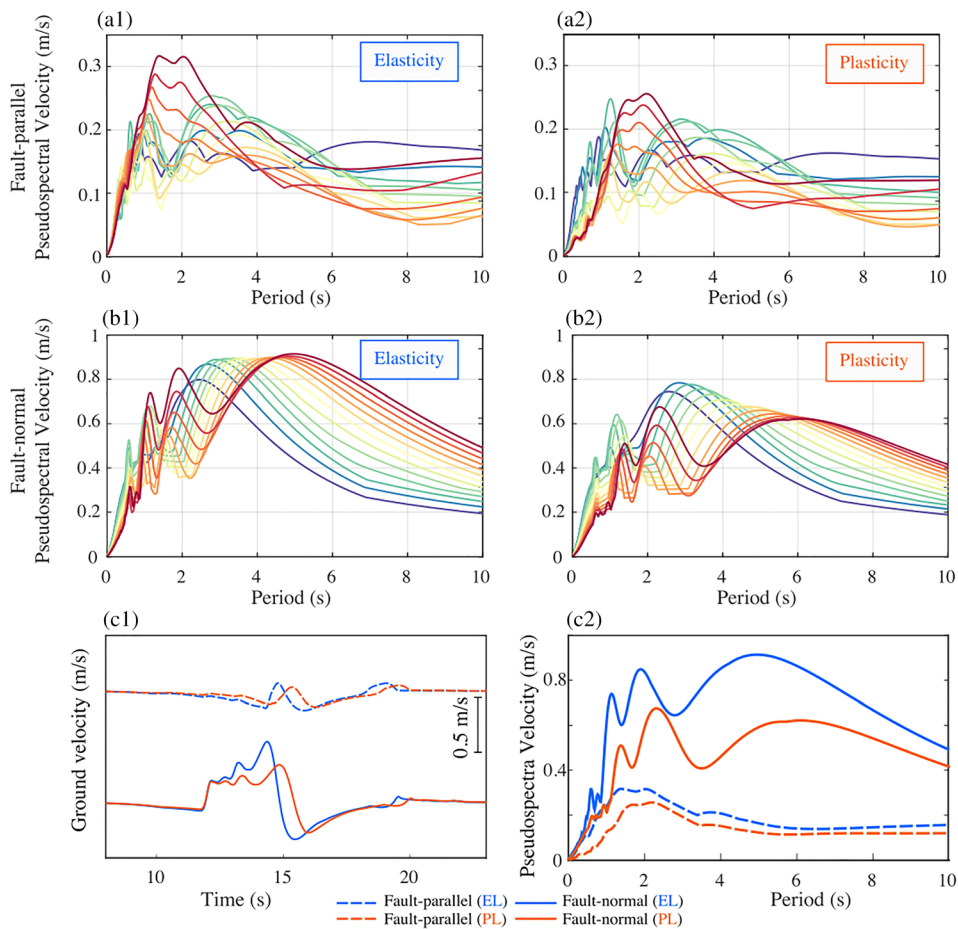


Figure 13. (a) Fault-parallel and (b) fault-normal pseudospectral velocities in both elastic and plastic cases in the self-healing rupture scenarios. (c) Fault-parallel and fault-normal velocities at the most distant station (dark red triangle in Figure 6a), and their pseudospectral velocities.

Heaton (2008). However, the modifications due to plastic yielding remain much the same as we found in sections 4 and 5. Figure 13c1, compared with Figure 7c, shows more localized, smaller peaks preceding the largest one (and also a lower peak amplitude, as expected in light of the lower moment for the self-healing model). Figure 13b shows that multiple prominent short-period peaks (especially around 2 s) in the PSV start to develop with increasing along-strike distance (over 25 km of epicentral distance) and at the most distant station (40 km away) these shorter-period peaks approach the level of the primary peak corresponding to the dominant pulse duration (~ 5 s). This behavior is consistent with what we found in the rough fault scenario (section 5) and is likewise in agreement with the results of Aagaard and Heaton (2008) that self-healing rupture compacts and splits the directivity-induced FN pulse, enriching the short-period content (see their Figure 9) while preserving the long-period pulse. Moreover, the fault-parallel PSV starts to display a systematic peak (also at ~ 2 s, see Figure 13a), which is associated with a relatively impulsive fault-parallel velocity (Figure 13c1). The prominent short-period peaks corresponding to the localized short rise time from self-healing procedures are similarly found in the rough fault scenario.

Off-fault plasticity influences the directivity pulse in self-healing rupture in essentially the same manner as was the case for the planar and rough fault models discussed earlier. As seen in Figures 13c1 and 13c2, the directivity pulse in the plastic case becomes weaker and broader, and short- and long-period PSV peaks (1.5, 2, and 5 s) are accordingly shifted in period and reduced in amplitude at the more distance stations, where relatively large strains occur. That is, the stations with greater epicenter distance experience more attenuation of the long-period motion that controls the PSV peak (Figure 13b2), which again

results in an along-strike saturation of near-fault directivity-induced amplification in the long-period band (Figure S10).

6.2. Implications for Directivity Models Used in Ground-Motion Prediction

6.2.1. Directivity in Empirical Models

A number of modifications to empirical GMPE have been proposed to account for rupture directivity and the strong FN pulse (e.g., Rowshandel, 2010; Somerville et al., 1997; Spudich et al., 2014; Spudich & Chiou, 2008). As an example for this process, Somerville et al. (1997) introduced (e.g., in the strike-slip case) directivity parameter ($X\cos\theta$), with X representing the proportion of the fault rupture distance that is toward a site of interest and θ representing the effect of the radiation direction relative to the fault strike. Abrahamson (2000) later modified the model such that the predicted effect saturates for directivity parameters larger than 0.4 and the directivity effect is further reduced through the use of tapers for off-fault distance >30 km (distance taper) and magnitude <6.5 (magnitude taper). With far larger data sets available (e.g., NGA-West2), more recent models have introduced a number of improvements. The parameterization using normalized rupture length X is now recognized as nonphysical (e.g., Bayless & Somerville, 2013). In the NGA-West2 directivity models (Bayless & Somerville, 2013; Chiou & Spudich, 2013; Rowshandel, 2013; Shahi & Baker, 2013; Spudich & Chiou, 2013), the absolute rupture dimension (toward the site) in km is adopted instead. Moreover, all models except the model of Bayless and Somerville (2013) are now explicitly “narrow-band” models in which the directivity-induced amplification (of response spectra) peaks at a specific period and decreases away from the peak on both sides of the peak. The peak period roughly scales with magnitude, which is consistent with the dependence of pulse period on earthquake magnitude in the NGA-West2 data set (Shahi & Baker, 2014; Somerville, 2003).

Our simulation results in the foregoing sections essentially support the two aforementioned features of recent empirical directivity models. That is, the simulated directivity-induced amplification wedge (i.e., the amplified zone in an acute angle about the rupture propagation direction) mirrors the empirical-model dependence on the fault rupture length, and the period dependence of that amplification is narrow band. However, our models of directivity-induced amplification, in both 3-D elastic and plastic scenarios, demonstrate greater along-strike and off-fault distance- and period-dependent variability of directivity effects and these dependences are inherently intertwined.

6.2.2. Spatial Dependence

First, we discuss the spatial features of directivity-induced amplification. Contours of the directivity amplification adjustment in GMMs are wedge shaped in the near-fault area, as shown in background color of Figure 1, in which the directivity-induced amplification increases with along-strike distance. A result is that all directivity models tend to predict that big ground motions occur in a broad zone off the end of fault. However, as found in the 1992 Landers earthquake, the big ground motion records that excited interest in the directivity pulse in ground motions, like the Lucerne recording, are likely to occur at short rupture distances relative to the total rupture length. Our elastic and plastic simulations may shed some light on this issue. In all of our elastic scenarios (including those where the slip pulse is geometrically induced on planar (section 4) or rough (section 5) fault surfaces, and those where the rupture is self-healing (section 6.1), the spatial pattern of directivity-induced amplification is period dependent. The long-period contours are wedge shaped, consistent with directivity models recently developed. In contrast, the maximal motions in the short- and intermediate-period band are very localized near the fault trace and controlled by short-period behaviors of the passing rupture.

The off-fault plasticity, as previously noted, can limit growth of the long-period PSA with the along-strike distance, consistent with a directivity amplification adjustment model, which includes the along-strike distance truncation (Abrahamson, 2000). As in Figure 12b3, the maximal long-period PSA is located nearly 25 km from the epicenter. The FN width measured by the FN distance to a given PSA contour (here we choose 1.8 m/s^2 for illustration) reaches a maximum (roughly 8 km in Figure 12b3) and then remains essentially constant, which in our simulations demonstrates that the plastic yielding truncates the along-strike and FN growth of directivity amplification. Thus, our simulations may provide guidance for parameterizing distance tapers used in GMMs.

In directivity models, the FN width of high-directivity zones is controlled by rather poorly constrained distance tapers. As suggested by the foregoing simulations, this taper should be a function of period,

but very few models currently consider this issue (of those cited above, only Rowshandel, 2013, addresses this issue). On the other hand, due to insufficient near-fault (within 10 km) data coverage, the empirical directivity models thus derived may overestimate ground motion in near-fault area. Our plastic simulations in section 4 imply that PGV saturates (as a function of FN distance) at a level below 2 m/s, an effect not captured by elastic simulations (which can continue to increase above that level at distances less than 2 km or so). Simulations with plasticity also show PGV saturating as stress drop increases, and this stress drop saturation may be a component of magnitude saturation seen in the near-fault PGV (Baltay & Hanks, 2014; Schmedes & Archuleta, 2008). We caution that the quantitative results just cited (i.e., for both the saturation level and FN distance range in which it applies) will require refinement through better constrained cohesion models and more extensive parameter studies. But other recent work supports the concept of stress drop insensitivity of PGV within a near-fault range of the order of several km, and with a velocity saturation level within about 50% of our 2-m/s estimate. Further development of dynamic rupture simulations that include inelastic yielding can supplement near-fault constraints on directivity-induced amplification and have the potential to advance development of GMPE directivity models.

6.2.3. Pulse Period

Next, we explore the dependence of pulse period on typical GMPE parameters. Several empirical models have related the pulse period to earthquake magnitude, typically inferring almost a linear relationship (Shahi & Baker, 2014; Somerville, 2003), as seen in Figure 14b (where we replot the data from (Fayjaloun et al., 2017)). However, as suggested by Fayjaloun et al. (2017), the increase of pulse period with magnitude is implicitly expressed through the parameter D , defined as the length of the fault that ruptures toward the site (Figure 14a). The idea is that, for the strike-slip earthquakes that are the subject of this study, earthquake magnitude scales with rupture length, and therefore near-rupture recordings at large values of D can only occur for sufficiently long ruptures. Small values of D can also occur for long ruptures, but, for a random sample of near-rupture records, the mean D of the sample will be proportional to rupture length, and therefore to the event magnitude (Figure 7 in Fayjaloun et al., 2017). The D effect on pulse width is consistently present in our 2-D kinematic (section 2), 3-D planar (section 4), and rough fault (section 5) scenarios. In each case, the pulse period scales with rupture distance toward the site (D), in agreement with the proposed relationship of (Fayjaloun et al., 2017). The suggestion that the apparent magnitude dependence of pulse period actually reflects a dependence on rupture distance toward site (i.e., D) is highlighted in the comparison of Figure 14b with Figure 14c. In Figure 14b, the pulse-period data points for the 10 strike-slip earthquakes in Table 1 of Fayjaloun et al. (2017) are plotted versus magnitude, whereas in Figure 14c the same data have been plotted versus D . In Figure 14c, the pulse periods for each individual earthquake can be interpreted to follow a common scaling with D , most noticeably in the case of the 1999 Kocaeli and 1979 Imperial Valley earthquakes, for which the scatter of pulse periods with respect to a regression line D is smaller than with respect to one on magnitude. This comparison supports the view that the apparent magnitude scaling in Figure 14b results physically from scaling of period with D , combined with the natural correlation of magnitude with D .

The near-fault recording TTRH02 of the 2000 Tottori earthquake is also consistent with this view that pulse period is directly related to parameter D . The Tottori event resembles our simulations in rupture velocity (around 80–90% shear wave speed, Semmane et al., 2005) and hypocentral depth (~10 km, USGS and Iwata & Sekiguchi, 2002), while it is substantially lower in moment magnitude (most seismic moment estimates for the Tottori earthquake are lower than our simulation moments by a factor of four or more; see Semmane et al., 2005). Figure 14c compares The TTRH02 (borehole) FN velocity in the 2000 Tottori earthquake and our simulated FN velocity pulses on a geometrically rough fault (section 5) in elastic and plastic cases at a similar epicentral (~7 km) and off-fault distance (~1 km). Both elastic and plastic simulations follow the recorded velocity closely with respect to the timing of arrivals, and even their shapes (apart from the high simulated amplitude at the S wave onset, perhaps related to the artificial rupture initiation in the simulation). These arrivals include the prominent near-field P wave, the hypocentral S wave, and the pulse termination associated with healing following rupture passage, and the result is that there is close agreement with the recorded pulse duration at this distance (no filter applied). This agreement suggests that (in this case of a site very near the fault) pulse duration is relatively insensitivity to the source complexity, because (apart from the general similarities noted above) the simulations are not constrained by any Tottori event-specific

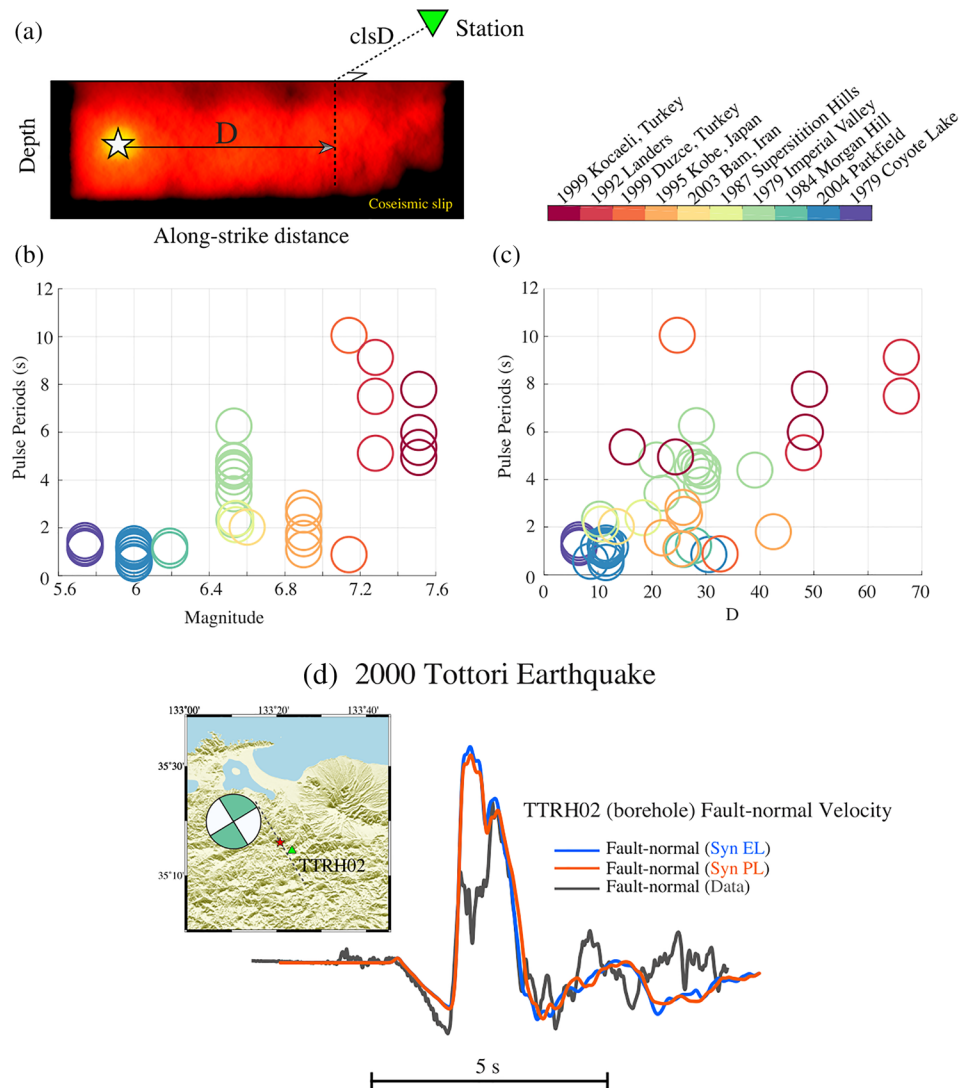


Figure 14. (a) Conceptual definition of rupture length parameter D and the length of the fault that ruptures toward the site. (b) The relationship between pulse periods and magnitudes of 10 strike-slip earthquakes. (c) The relationship between pulse periods and D for 10 strike-slip earthquakes. (d) Location map for the 2000 Tottori earthquake and the TTRH02 (borehole) site, and an observed fault-normal velocity trace TTRH02 compared with foregoing simulations on a geometrically rough fault in both elastic and plastic cases. Simulated fault-normal velocities are retrieved at a site of consistent along-strike epicentral distance and off-fault distance of TTRH02.

information. The result is in agreement with the view that pulse period has primary dependency on the rupture distance parameter D .

The primary scaling of pulse period with D is common to each type of rupture model that we have considered, though there is some relatively weak model dependency. For example, our 3-D plastic simulations indicate that the off-fault plasticity can broaden the pulse to varying degrees, depending on the cumulated plastic strain. Moreover, in our simulated self-healing rupture, additional short-period pulses emerge, while nonetheless preserving the primary pulse duration dominated by scaling with D .

The inelastic effects seen in the simulations have their greatest effect at distances to the rupture of roughly 2 km or less. Therefore, inelastic effects will be especially important when rupture simulations are used to extrapolate directivity-pulse behavior to sites very near the rupture surface. Roten et al. (2014) suggest that a typical simulation assuming a linear response of rock will overpredict ground motions during potential large earthquakes on the southern San Andreas Fault (e.g., Cybershake). The effects of plasticity depend on the cohesion values used, are also sensitive to a presence of a low-velocity fault damage zone (Roten,

Olsen, Day, & Cui, 2017). The results we have presented can provide guidance on the general spatial and period dependencies to be expected for pulses in the near-rupture regime, while much scope remains to use rupture simulations to better quantify those dependencies and their variability.

6.3. Some Limitations of the Study

The effect of plastic yielding depends upon the cohesion values used. We chose a depth-independent cohesion value of 3 MPa because (1) this value is typically within the range of empirical estimates based on sedimentary rock strength (e.g., Chang et al., 2006) and (2) the value is large enough that it permits inelastic effects to be modeled without substantially impacting dynamics (e.g., stress drop, magnitude, and rupture velocity) of the simulated earthquakes. This approach allows us to isolate and interpret plasticity effects on directivity pulses and provide general guidance as to expected plasticity effects on the spatial distribution, spectral characteristics, and scaling of those pulses. However, this approach is not a substitute for simulations based upon region- and site-specific cohesion models when that is possible. As noted by, for example, Roten et al. (2014), cohesion may vary over several orders of magnitude, from nearly 0 in sedimentary rock to hundreds of MPa crystalline rock at seismogenic depth, and the neglect of depth-dependent cohesion may underpredict inelastic effects, especially if shallow low-cohesion cohesionless sedimentary rock is present. Whereas, the found fundamental qualitative results due to plasticity (broadened pulse and reduced amplitude) is insensitive to the chosen value that quantitatively affects the degree of plastic impacts, as long as plastic damping occurs.

The DP model used in our simulations applies a pressure-dependent strength limit while remaining sufficiently simple that the simulations can be understood and interpreted relatively easily. This model neglects several effects whose significance should be explored in future studies, however. The DP model neglects possible strain hardening and softening, for example. Inappropriate neglect of hardening might lead to overprediction of the amount of nonlinear damping in soil and soft rocks, resulting in a corresponding underprediction of ground motion metrics. In addition, laboratory experiments on soils and soft rocks imply a more complex nonlinear behavior (e.g., gradual reduction of the shear modulus, Hardin & Drnevich, 1972) that is not considered in perfectly plastic models such as DP, potentially leading to an overprediction of ground motions. As an improvement in the 3-D modeling of nonlinear soil response, Roten et al. (2019) implements an Iwan-type plasticity model in ground motions simulations in Los Angeles Basin, which reproduces Masing reloading and unloading behavior by tracking an overlay of individual von Mises yield surfaces (mimicking a realistic hyperbolic yield surface). While those simulations do not focus specifically on the long-period directivity pulses considered here, they do underscore the importance of nonlinear effects for long-period (greater than 1-s period) ground motion in general, and they confirm that the Iwan model, through hystereric damping, attenuates long-period ground motions more than does the DP model (when both models impose the same shear stress limit).

Brittle damage, another style of inelasticity in rock, differs from plasticity, and it will be of interest to reexamine directivity pulses in simulations that include damage. Both plasticity and brittle damage limit stress at high strain, but a key difference between these two rheologies is that brittle damage changes the elastic moduli of the yielding material while plasticity does not. Dynamic changes of elastic moduli have been well documented in laboratory experiments (e.g., Aben et al., 2019; Gupta, 1973; Hamiel et al., 2004; Lockner et al., 1977; Zoback & Byerlee, 1975). Therefore, brittle damage may generate a low-velocity damage zone surrounding the fault surface, which may in turn amplify near-fault ground motions (Spudich & Olsen, 2001). Various brittle damage models have been derived, in an effort to account for effects such as tensile microfractures and solid-granular transitions (e.g., Yamashita, 2000; Dalguer, 2003; Dalguer et al., 2003; Bhat et al., 2012; Lyakhovsky & Ben-Zion, 2014; Xu et al., 2015; Thomas & Bhat, 2018).

7. Conclusions

Plastic yielding, which is absent in conventional kinematic models, can systematically affect the amplitude, frequency content and distance scaling of near-fault directivity pulses. Three-dimensional dynamic strike-slip simulations confirm the importance of yielding for both planar and rough fault models as well as for self-healing models. These models (scaled to $\sim M 7$) consistently predict FN pulse similar to the observed (period of 2–5 s, amplitudes increasing with rupture distance until reaching a limit), but the pulse shapes are systematically modified (relative to the elastic cases) by the off-fault plasticity, through a

reduction of peak velocity and increase of dominant period. Moreover, off-fault plastic yielding causes near-fault ($< \sim 2$ km) PGV to saturate with respect to increases in both stress drop and rupture distance toward the site, which may contribute to the observed magnitude saturation of near-fault PGV. These results support incorporation of the following elements into empirical directivity pulse models: (i) a FN distance saturation factor, (ii) a period-dependent and along-strike distance-dependent factor representing directivity, and (iii) an along-strike saturation factor to truncate growth of the directivity factor. Off-fault plasticity is also found to strongly suppress the otherwise very strong high-frequency fault-parallel acceleration pulses associated with rupture breakout at the free surface. Taken together, the results discussed here underscore the importance of including off-fault inelastic response in rupture modeling intended to guide the formulation of empirical GMMs, especially when rupture simulations are used to extrapolate empirical models to sites very near the rupture surface.

Data Availability Statement

Figures were prepared using MATLAB (<https://www.mathworks.com>) and the Generic Mapping Tools (<http://gmt.soest.hawaii.edu>). The TTRH02 (borehole) record was from the Japanese KiK-net database. The pulse durations of the simulated near-fault velocities were computed using the Shahi and Baker (2014) algorithm (MATLAB computer code available at <https://github.com/shreyshahi/PulseClassification>). Pulse periods, seismic moments, rupture distances of 10 representative strike-slip earthquakes were extracted and reorganized from Table 1 and Table A1 of Fayjaloun et al. (2017). The rupture dynamics code used in this paper can be assessed at the website (<https://figshare.com/articles/SORDlatest/10385249>). Software configuration files are accessible at the website (https://figshare.com/articles/Effects_of_off-fault_inelasticity_on_near-fault_directivity_pulses/10385186).

Acknowledgments

The authors tremendously appreciate two anonymous reviewers and Associate Editor Alice Gabriel who altogether fruitfully improved this manuscript. This research was supported through Grant 18204 of the Southern California Earthquake Center (SCEC) funded by the National Science Foundation (NSF) Cooperative Agreement EAR-1033462 and U.S. Geological Survey (USGS) Cooperative Agreement G12AC20038. The work was also supported by an award of computer time provided by the Innovative and Novel Computational Impact on Theory and Experiment (INCITE) program, through projects GMSeismicSim and SeismicHazard2 of the Southern California Earthquake Center. This research used resources of the Argonne Leadership Computing Facility, which is a DOE Office of Science User Facility supported under Contract DE-AC02-06CH11357.

References

- Aagaard, B. T., & Heaton, T. H. (2004). Near-source ground motions from simulations of sustained intersonic and supersonic fault ruptures. *Bulletin of the Seismological Society of America*, 94(6), 2064–2078. <https://doi.org/10.1785/0120030249>
- Aagaard, B. T., & Heaton, T. H. (2008). Constraining fault constitutive behavior with slip and stress heterogeneity. *Journal of Geophysical Research*, 113, B04301. <https://doi.org/10.1029/2006jb004793>
- Aagaard, B. T., Heaton, T. H., & Hall, J. F. (2001). Dynamic earthquake ruptures in the presence of lithostatic normal stresses: Implications for friction models and heat production. *Bulletin of the Seismological Society of America*, 91(6), 1765–1796. <https://doi.org/10.1785/0120000257>
- Aben, F. M., Brantut, N., Mitchell, T. M., & David, E. C. (2019). Rupture energetics in crustal rock from laboratory-scale seismic tomography. *Geophysical Research Letters*, 46, 7337–7344. <https://doi.org/10.1029/2019GL083040>
- Abrahamson, N. A. (2000). Effects of rupture directivity on probabilistic seismic hazard analysis. *Proceedings of the sixth international conference on seismic zonation*. Earthquake Engineering Research Institute, Oakland, CA.
- Aki, K., & Richards, P. G. (2002). *Quantitative seismology*. Sausalito, CA: University Science Books.
- Anderson, J. C., & Bertero, V. V. (1987). Uncertainties in establishing design earthquakes. *Journal of Structural Engineering-Asce*, 113(8), 1709–1724. [https://doi.org/10.1061/\(ASCE\)0733-9445\(1987\)113:8\(1709\)](https://doi.org/10.1061/(ASCE)0733-9445(1987)113:8(1709))
- Andrews, D. J. (2005). Rupture dynamics with energy loss outside the slip zone. *Journal of Geophysical Research*, 110, B01307. <https://doi.org/10.1029/2004JB003191>
- Andrews, D. J., & Barall, M. (2011). Specifying initial stress for dynamic heterogeneous earthquake source models. *Bulletin of the Seismological Society of America*, 101(5), 2408–2417. <https://doi.org/10.1785/0120110012>
- Archuleta, R. J., & Hartzell, S. H. (1981). Effects of fault finiteness on near-source ground motion. *Bulletin of the Seismological Society of America*, 71(4), 939–957.
- Baker, J. W. (2007). Quantitative classification of near-fault ground motions using wavelet analysis. *Bulletin of the Seismological Society of America*, 97(5), 1486–1501. <https://doi.org/10.1785/0120060255>
- Baltay, A., & Hanks, T. (2014). Understanding the magnitude dependence of PGA and PGV in NGA-West 2 data. *Bulletin of the Seismological Society of America*, 104(6), 2851–2865. <https://doi.org/10.1785/0120130283>
- Baltay, A. S., & Boatwright, J. (2015). Ground-motion observations of the 2014 South Napa earthquake. *Seismological Research Letters*, 86(2A), 355–360. <https://doi.org/10.1785/0220140232>
- Baumann, C., & Dalguer, L. A. (2014). Evaluating the compatibility of dynamic rupture-based synthetic ground motion with empirical ground-motion prediction equation. *Bulletin of the Seismological Society of America*, 104(2), 634–652. <https://doi.org/10.1785/0120130077>
- Bayless, J. R., & Somerville, P. G. (2013). Final Report of the NGA-West2 Directivity Working Group, Chapter 2Rep., Pacific Earthquake Engineering Research Center, University of California, Berkeley, CA.
- Ben-Zion, Y., Rockwell, T. K., Shi, Z. Q., & Xu, S. Q. (2012). Reversed-polarity secondary deformation structures near fault stepovers. *Journal of Applied Mechanics*, 79(3), 031025. <https://doi.org/10.1115/1.4006154>
- Ben-Zion, Y., & Sammis, C. G. (2003). Characterization of fault zones. *Pure and Applied Geophysics*, 160(3), 677–715. <https://doi.org/10.1007/pl00012554>
- Beroza, G. C., & Mikumo, T. (1996). Short slip duration in dynamic rupture in the presence of heterogeneous fault properties. *Journal of Geophysical Research*, 101(B10), 22449–22460. <https://doi.org/10.1029/96JB02291>
- Bertero, V. V., Mahin, S. A., & Herrera, R. A. (1978). Aseismic design implications of near-fault San-Fernando earthquake records. *Earthquake Engineering and Structural Dynamics*, 6(1), 31–42. <https://doi.org/10.1002/eqe.4290060105>

- Bhat, H. S., Rosakis, A. J., & Sammis, C. G. (2012). A micromechanics based constitutive model for brittle failure at high strain rates. *Journal of Applied Mechanics*, 79(3), https://doi.org/10.1115/1.4005897
- Bizzarri, A., Dunham, E. M., & Spudich, P. (2010). Coherence of Mach fronts during heterogeneous supershear earthquake rupture propagation: Simulations and comparison with observations. *Journal of Geophysical Research*, 115, B08301. https://doi.org/10.1029/2009JB006819
- Boatwright, J., & Boore, D. M. (1975). Simplification in calculation of motions near a propagating dislocation. *Bulletin of the Seismological Society of America*, 65(1), 133–138.
- Boore, D. M. (2010). Orientation-independent, nongeometric-mean measures of seismic intensity from two horizontal components of motion. *Bulletin of the Seismological Society of America*, 100(4), 1830–1835. https://doi.org/10.1785/0120090400
- Boore, D. M., Aki, K., & Todd, T. (1971). A two-dimensional moving dislocation model for a strike-slip fault. *Bulletin of the Seismological Society of America*, 61(1), 177–194.
- Boore, D. M., & Atkinson, G. M. (2008). Ground-motion prediction equations for the average horizontal component of PGA, PGV, and 5%-damped PSA at spectral periods between 0.01 s and 10.0 s. *Earthquake Spectra*, 24(1), 99–138. https://doi.org/10.1193/1.2830434
- Boore, D. M., Watson-Lamprey, J., & Abrahamson, N. A. (2006). Orientation-independent measures of ground motion. *Bulletin of the Seismological Society of America*, 96(4A), 1502–1511. https://doi.org/10.1785/0120050209
- Boore, D. M., & Zoback, M. D. (1974). Near-field motions from kinematic models of propagating faults. *Bulletin of the Seismological Society of America*, 64(2), 321–342.
- Bozorgnia, Y., Abrahamson, N. A., Atik, L. A., Ancheta, T. D., Atkinson, G. M., Baker, J. W., et al. (2014). NGA-West2 research project. *Earthquake Spectra*, 30(3), 973–987. https://doi.org/10.1193/072113eqs209m
- Bozorgnia, Y., & Campbell, A. (2004). Engineering characterization of ground motion. In *Earthquake engineering: From engineering seismology to performance-based engineering*. Boca Raton, FL: CRC Press.
- Broberg, K. B. (1996). How fast can a crack go? *Materials Science*, 32(1), 80–86. https://doi.org/10.1007/Bf02538928
- Broberg, K. B. (1999). Intersonic mode II crack acceleration. *Fatigue & Fracture of Engineering Materials & Structures*, 22(1), 17–24. https://doi.org/10.1046/j.1460-2695.1999.00129.x
- Brooks, B. A., Minson, S. E., Glennie, C. L., Nevitt, J. M., Dawson, T., Rubin, R., et al. (2017). Buried shallow fault slip from the South Napa earthquake revealed by near-field geodesy. *Science Advances*, 3(7), e1700525. https://doi.org/10.1126/sciadv.1700525
- Candela, T., Renard, F., Bouchon, M., Brouste, A., Marsan, D., Schmittbuhl, J., & Voisin, C. (2009). Characterization of fault roughness at various scales: Implications of three-dimensional high resolution topography measurements. *Pure and Applied Geophysics*, 166(10–11), 1817–1851. https://doi.org/10.1007/s00024-009-0521-2
- Chang, C. D., Zoback, M. D., & Khaksar, A. (2006). Empirical relations between rock strength and physical properties in sedimentary rocks. *Journal of Petroleum Science and Engineering*, 51(3–4), 223–237. https://doi.org/10.1016/j.petrol.2006.01.003
- Chiou, B. S. J., & Spudich, P. (2013). Final Report of the NGA-West2 Directivity Working Group, Chapter 6Rep., Pacific Earthquake Engineering Research Center, University of California, Berkeley, CA.
- Dalguer, L. A. (2003). Generation of new cracks accompanied by the dynamic shear rupture propagation of the 2000 Tottori (Japan) Earthquake. *Bulletin of the Seismological Society of America*, 93(5), 2236–2252. https://doi.org/10.1785/0120020171
- Dalguer, L. A., Irikura, K., & Riera, J. D. (2003). Simulation of tensile crack generation by three-dimensional dynamic shear rupture propagation during an earthquake. *Journal of Geophysical Research: Solid Earth*, 108(B3), https://doi.org/10.1029/2001jb001738
- Das, S. (2015). Supershear earthquake ruptures—Theory, methods, laboratory experiments and fault superhighways: An update. *Perspectives on European Earthquake Engineering and Seismology*, 39, 1–20. https://doi.org/10.1007/978-3-319-16964-4_1
- Day, S. M. (1982). Three-dimensional finite difference simulation of fault dynamics: Rectangular faults with fixed rupture velocity. *Bulletin of the Seismological Society of America*, 72(3), 705–727.
- Day, S. M., Dalguer, L. A., Lapusta, N., & Liu, Y. (2005). Comparison of finite difference and boundary integral solutions to three-dimensional spontaneous rupture. *Journal of Geophysical Research*, 110, B12307. https://doi.org/10.1029/2005JB003813
- Day, S. M., & Ely, G. P. (2002). Effect of a shallow weak zone on fault rupture: Numerical simulation of scale-model experiments. *Bulletin of the Seismological Society of America*, 92(8), 3022–3041. https://doi.org/10.1785/0120010273
- Day, S. M., Gonzalez, S. H., Anooshehpour, R., & Brune, J. N. (2008). Scale-model and numerical simulations of near-fault seismic directivity. *Bulletin of the Seismological Society of America*, 98(3), 1186–1206. https://doi.org/10.1785/0120070190
- Donahue, J., Stewart, J., Gregor, N., & Bozorgnia, Y. (2019). Ground-motion directivity modeling for seismic hazard applications Rep., Pacific Earthquake Engineering Research Center Headquarters at the University of California, Berkeley.
- Douglas, A., Hudson, J. A., & Pearce, R. G. (1988). Directivity and the Doppler-effect. *Bulletin of the Seismological Society of America*, 78(3), 1367–1372.
- Drucker, D. C., & Prager, W. (1952). Soil mechanics and plastic analysis or limit design. *Quarterly of Applied Mathematics*, 10(2), 157–165. https://doi.org/10.1090/qam/48291
- Duan, B., & Day, S. M. (2008). Inelastic strain distribution and seismic radiation from rupture of a fault kink. *Journal of Geophysical Research*, 113, B12311. https://doi.org/10.1029/2008JB005847
- Dunham, E. M., Belanger, D., Cong, L., & Kozdon, J. E. (2011a). Earthquake ruptures with strongly rate-weakening friction and off-fault plasticity, Part 1: Planar faults. *Bulletin of the Seismological Society of America*, 101(5), 2296–2307. https://doi.org/10.1785/0120100075
- Dunham, E. M., Belanger, D., Cong, L., & Kozdon, J. E. (2011b). Earthquake ruptures with strongly rate-weakening friction and off-fault plasticity, Part 2: Nonplanar faults. *Bulletin of the Seismological Society of America*, 101(5), 2308–2322. https://doi.org/10.1785/0120100076
- Dunham, E. M., & Bhat, H. S. (2008). Attenuation of radiated ground motion and stresses from three-dimensional supershear ruptures. *Journal of Geophysical Research*, 113, B08319. https://doi.org/10.1029/2007JB005182
- Ely, G. P., Day, S. M., & Minster, J.-B. (2008). A support-operator method for viscoelastic wave modelling in 3-D heterogeneous media. *Geophysical Journal International*, 172(1), 331–344. https://doi.org/10.1111/j.1365-246X.2007.03633.x
- Ely, G. P., Day, S. M., & Minster, J.-B. (2009). A support-operator method for 3-D rupture dynamics. *Geophysical Journal International*, 177(3), 1140–1150. https://doi.org/10.1111/j.1365-246X.2009.04117.x
- Ely, G. P., Day, S. M., & Minster, J.-B. (2010). Dynamic rupture models for the southern San Andreas Fault. *Bulletin of the Seismological Society of America*, 100(1), 131–150. https://doi.org/10.1785/0120090187
- Erickson, B. A., Dunham, E. M., & Khosrovifar, A. (2017). A finite difference method for off-fault plasticity throughout the earthquake cycle. *Journal of the Mechanics and Physics of Solids*, 109, 50–77. https://doi.org/10.1016/j.jmps.2017.08.002
- Fang, Z. J., & Dunham, E. M. (2013). Additional shear resistance from fault roughness and stress levels on geometrically complex faults. *Journal of Geophysical Research-Solid Earth*, 118, 3642–3654. https://doi.org/10.1002/jgrb.50262

- Fayjaloun, R., Causse, M., Voisin, C., Cornou, C., & Cotton, F. (2017). Spatial variability of the directivity pulse periods observed during an earthquake. *Bulletin of the Seismological Society of America*, 107(1), 308–318. <https://doi.org/10.1785/0120160199>
- Fialko, Y., Sandwell, D., Simons, M., & Rosen, P. (2005). Three-dimensional deformation caused by the Bam, Iran, earthquake and the origin of shallow slip deficit. *Nature*, 435(7040), 295–299. <https://doi.org/10.1038/nature03425>
- Finn, W. D. L., Ventura, C. E., & Schuster, N. D. (1995). Ground motions during the 1994 Northridge earthquake. *Canadian Journal of Civil Engineering*, 22(2), 300–315. <https://doi.org/10.1139/l95-044>
- Gallovin, F. (2016). Modeling velocity recordings of the Mw 6.0 South Napa, California, earthquake: Unilateral event with weak high-frequency directivity. *Seismological Research Letters*, 87(1), 2–14. <https://doi.org/10.1785/0220150042>
- Goldsby, D. L., & Tullis, T. E. (2011). Flash heating leads to low frictional strength of crustal rocks at earthquake slip rates. *Science*, 334(6053), 216–218. <https://doi.org/10.1126/science.1207902>
- Gritz, A. (2009). Effect of heterogeneous prestress on near-field rupture directivity, MS thesis, San Diego State University.
- Gupta, I. N. (1973). Seismic velocities in rock subjected to axial loading up to SHEAR fracture. *Journal of Geophysical Research*, 78(29), 6936–6942. <https://doi.org/10.1029/JB078i029p06936>
- Hall, J. F., Heaton, T. H., Halling, M. W., & Wald, D. J. (1995). Near-source ground motion and its effects on flexible buildings. *Earthquake Spectra*, 11(4), 569–605. <https://doi.org/10.1193/1.1585828>
- Hamiel, Y., Liu, Y. F., Lyakhovsky, V., Ben-Zion, Y., & Lockner, D. (2004). A viscoelastic damage model with applications to stable and unstable fracturing. *Geophysical Journal International*, 159(3), 1155–1165. <https://doi.org/10.1111/j.1365-246X.2004.02452.x>
- Hardin, B. O., & Drnevich, V. P. (1972). Shear modulus and damping in soils: design equations and curves. *Journal of Soil Mechanics & Foundations Division*, 98(sm7).
- Harris, R. A., Barall, M., Aagaard, B., Ma, S., Roten, D., Olsen, K., et al. (2018). A suite of exercises for verifying dynamic earthquake rupture codes. *Seismological Research Letters*, 89(3), 1146–1162. <https://doi.org/10.1785/0220170222>
- Harris, R. A., Barall, M., Archuleta, R., Dunham, E., Aagaard, B., Ampuero, J. P., et al. (2009). The SCEC/USGS dynamic earthquake rupture code verification exercise. *Seismological Research Letters*, 80(1), 119–126. <https://doi.org/10.1785/gssrl.80.1.119>
- Haskell, N. A. (1969). Elastic displacements in near-field of a propagating fault. *Bulletin of the Seismological Society of America*, 59(2), 865–908.
- Heaton, T. H. (1982). The 1971 San Fernando earthquake: A double event? *Bulletin of the Seismological Society of America*, 72(6), 2037–2062.
- Heaton, T. H. (1990). Evidence for and implications of self-healing pulses of slip in earthquake rupture. *Physics of the Earth and Planetary Interiors*, 64(1), 1–20. [https://doi.org/10.1016/0031-9201\(90\)90002-F](https://doi.org/10.1016/0031-9201(90)90002-F)
- Heaton, T. H., Hall, J. F., Wald, D. J., & Halling, M. W. (1995). Response of highrise and base-isolated buildings to a hypothetical Mw 7.0 blind thrust earthquake. *Science*, 267(5195), 206–211. <https://doi.org/10.1126/science.267.5195.206>
- Hirakawa, E., & Ma, S. (2016). Dynamic fault weakening and strengthening by gouge compaction and dilatancy in a fluid-saturated fault zone. *Journal of Geophysical Research-Solid Earth*, 121, 5988–6008. <https://doi.org/10.1002/2015JB012509>
- Huang, Y. H., & Ampuero, J. P. (2011). Pulse-like ruptures induced by low-velocity fault zones. *Journal of Geophysical Research*, 116, B12307. <https://doi.org/10.1029/2011JB008684>
- Iwata, T., & Sekiguchi, H. (2002). Source process and near-source ground motion during the 2000 Tottori-ken Seibu earthquake, paper presented at 11th Japan Earthquake Engineering Symposium, Earthquake Eng. Res. Liaison Comm., Sci. Counc. of Jpn., Tokyo.
- Kaneko, Y., & Fialko, Y. (2011). Shallow slip deficit due to large strike-slip earthquakes in dynamic rupture simulations with elasto-plastic off-fault response. *Geophysical Journal International*, 186(3), 1389–1403. <https://doi.org/10.1111/j.1365-246X.2011.05117.x>
- Kaneko, Y., & Lapusta, N. (2010). Supershear transition due to a free surface in 3-D simulations of spontaneous dynamic rupture on vertical strike-slip faults. *Tectonophysics*, 493(3–4), 272–284. <https://doi.org/10.1016/j.tecto.2010.06.015>
- Kaneko, Y., Lapusta, N., & Ampuero, J. P. (2008). Spectral element modeling of spontaneous earthquake rupture on rate and state faults: Effect of velocity-strengthening friction at shallow depths. *Journal of Geophysical Research*, 113, B09317. <https://doi.org/10.1029/2007JB005553>
- Kieling, K., Wang, R. J., & Hainzl, S. (2014). Broadband ground-motion simulation using energy-constrained rise-time scaling. *Bulletin of the Seismological Society of America*, 104(6), 2683–2697. <https://doi.org/10.1785/0120140063>
- Klinger, Y., Okubo, K., Vallage, A., Champenois, J., Delorme, A., Rougier, E., et al. (2018). Earthquake damage patterns resolve complex rupture processes. *Geophysical Research Letters*, 45, 10,279–10,287. <https://doi.org/10.1029/2018GL078842>
- Lindsey, E. O., Fialko, Y., Bock, Y., Sandwell, D. T., & Bilham, R. (2014). Localized and distributed creep along the southern San Andreas Fault. *Journal of Geophysical Research: Solid Earth*, 119, 7909–7922. <https://doi.org/10.1002/2014JB011275>
- Lockner, D. A., Walsh, J. B., & Byerlee, J. D. (1977). Changes in seismic velocity and attenuation during deformation of granite. *Journal of Geophysical Research*, 82(33), 5374–5378. <https://doi.org/10.1029/JB082i033p05374>
- Lu, X., Lapusta, N., & Rosakis, A. J. (2010). Pulse-like and crack-like dynamic shear ruptures on frictional interfaces: Experimental evidence, numerical modeling, and implications. *International Journal of Fracture*, 163(1–2), 27–39. <https://doi.org/10.1007/s10704-010-9479-4>
- Lyakhovsky, V., & Ben-Zion, Y. (2014). Damage-breakage rheology model and solid-granular transition near brittle instability. *Journal of the Mechanics and Physics of Solids*, 64, 184–197. <https://doi.org/10.1016/j.jmps.2013.11.007>
- Ma, S. (2008). A physical model for widespread near-surface and fault zone damage induced by earthquakes. *Geochemistry, Geophysics, Geosystems*, 9, Q11009. <https://doi.org/10.1029/2008GC002231>
- Ma, S., & Hirakawa, E. T. (2013). Dynamic wedge failure reveals anomalous energy radiation of shallow subduction earthquakes. *Earth and Planetary Science Letters*, 375, 113–122. <https://doi.org/10.1016/j.epsl.2013.05.016>
- Madariaga, R. (1977). High-frequency radiation from crack (stress drop) models of earthquake faulting. *Geophysical Journal of the Royal Astronomical Society*, 51(3), 625–651. <https://doi.org/10.1111/j.1365-246X.1977.tb04211.x>
- Mai, P., Galis, M., Thingbaijam, K., Vyas, J., & Dunham, E. (2017). Accounting for fault roughness in pseudo-dynamic ground-motion simulations. *Pure and Applied Geophysics*, 174(9), 3419–3450. <https://doi.org/10.1007/s00024-017-1536-8>
- Marone, C. (1998). Laboratory-derived friction laws and their application to seismic faulting. *Annual Review of Earth and Planetary Sciences*, 26(1), 643–696. <https://doi.org/10.1146/annurev.earth.26.1.643>
- Marone, C. J., Scholtz, C. H., & Bilham, R. (1991). On the mechanics of earthquake afterslip. *Journal of Geophysical Research*, 96(B5), 8441–8452. <https://doi.org/10.1029/91JB00275>
- Melgar, D., & Hayes, G. P. (2017). Systematic observations of the slip pulse properties of large earthquake ruptures. *Geophysical Research Letters*, 44, 9691–9698. <https://doi.org/10.1002/2017GL074916>
- Milliner, C. W. D., Dolan, J. F., Hollingsworth, J., Leprince, S., & Ayoub, F. (2016). Comparison of coseismic near-field and off-fault surface deformation patterns of the 1992 Mw 7.3 Landers and 1999 Mw 7.1 Hector Mine earthquakes: Implications for controls on the distribution of surface strain. *Geophysical Research Letters*, 43, 10,115–10,124. <https://doi.org/10.1002/2016GL069841>

- Milliner, C. W. D., Dolan, J. F., Hollingsworth, J., Leprince, S., Ayoub, F., & Sammis, C. G. (2015). Quantifying near-field and off-fault deformation patterns of the 1992 Mw 7.3 Landers earthquake. *Geochemistry, Geophysics, Geosystems*, 16, 1577–1598. <https://doi.org/10.1002/2014GC005693>
- Nielsen, S., & Madariaga, R. (2003). On the self-healing fracture mode. *Bulletin of the Seismological Society of America*, 93(6), 2375–2388. <https://doi.org/10.1785/0120020090>
- Noda, H., Dunham, E. M., & Rice, J. R. (2009). Earthquake ruptures with thermal weakening and the operation of major faults at low overall stress levels. *Journal of Geophysical Research*, 114, B07302. <https://doi.org/10.1029/2008JB006143>
- Passone, L., & Mai, P. M. (2017). Kinematic earthquake ground-motion simulations on listric normal faults. *Bulletin of the Seismological Society of America*, 107(6), 2980–2993. <https://doi.org/10.1785/0120170111>
- Perfettini, H., & Avouac, J. P. (2007). Modeling aftershocks and aftershocks following the 1992 Landers earthquake. *Journal of Geophysical Research*, 112, B07409. <https://doi.org/10.1029/2006JB004399>
- Power, W. L., & Tullis, T. E. (1991). Euclidean and fractal models for the description of rock surface-roughness. *Journal of Geophysical Research*, 96(B1), 415–424. <https://doi.org/10.1029/90JB02107>
- Renard, F., Voisin, C., Marsan, D., & Schmittbuhl, J. (2006). High resolution 3D laser scanner measurements of a strike-slip fault quantify its morphological anisotropy at all scales. *Geophysical Research Letters*, 33, L04305. <https://doi.org/10.1029/2005GL025038>
- Rice, J. R. (1992). Fault stress states, pore pressure distributions, and the weakness of the San Andreas fault. In *51 Fault mechanics and transport properties of rocks—A Festschrift in honor of W. F. Brace*, (pp. 475–503). San Diego: academic press. [https://doi.org/10.1016/s0074-6142\(08\)62835-1](https://doi.org/10.1016/s0074-6142(08)62835-1)
- Rice, J. R. (1993). Spatiotemporal complexity of slip on a fault. *Journal of Geophysical Research*, 98(B6), 9885–9907. <https://doi.org/10.1029/93JB00191>
- Rojas, O., Dunham, E. M., Day, S. M., Dalguer, L. A., & Castillo, J. E. (2009). Finite difference modelling of rupture propagation with strong velocity-weakening friction. *Geophysical Journal International*, 179(3), 1831–1858. <https://doi.org/10.1111/j.1365-246X.2009.04387.x>
- Roten, D., Olsen, K. B., & Day, S. M. (2017). Off-fault deformations and shallow slip deficit from dynamic rupture simulations with fault zone plasticity. *Geophysical Research Letters*, 44, 7733–7742. <https://doi.org/10.1002/2017GL074323>
- Roten, D., Olsen, K. B., & Day, S. M. (2019). 3D simulation of Large San Andreas scenario earthquakes using a multi-surface plasticity model. *Seismological Research Letters*, 90(2B), 947.
- Roten, D., Olsen, K. B., Day, S. M., & Cui, Y. (2017). Quantification of fault-zone plasticity effects with spontaneous rupture simulations. *Pure and Applied Geophysics*, 174(9), 3369–3391. <https://doi.org/10.1007/s0024-017-1466-5>
- Roten, D., Olsen, K. B., Day, S. M., Cui, Y., & Fah, D. (2014). Expected seismic shaking in Los Angeles reduced by San Andreas fault zone plasticity. *Geophysical Research Letters*, 41, 2769–2777. <https://doi.org/10.1002/2014GL059411>
- Roten, D., Olsen, K. B., & Pechmann, J. C. (2012). 3D simulations of M7 earthquakes on the Wasatch Fault, Utah, Part II: Broadband (0–10 Hz) ground motions and nonlinear soil behavior. *Bulletin of the Seismological Society of America*, 102(5), 2008–2030. <https://doi.org/10.1785/0120110286>
- Rowhandel, B. (2010). Directivity correction for the next generation attenuation (NGA) relations. *Earthquake Spectra*, 26(2), 525–559. <https://doi.org/10.1193/1.3381043>
- Rowhandel, B. (2013). Final Report of the NGA-West2 Directivity Working Group, Chapter 3Rep., Pacific Earthquake Engineering Research Center, University of California, Berkeley, CA.
- Sagy, A., & Brodsky, E. E. (2009). Geometric and rheological asperities in an exposed fault zone. *Journal of Geophysical Research*, 114, B02301. <https://doi.org/10.1029/2008JB005701>
- Scala, A., Festa, G., & Del Gaudio, S. (2018). Relation between near-fault ground motion impulsive signals and source parameters. *Journal of Geophysical Research: Solid Earth*, 123, 7707–7721. <https://doi.org/10.1029/2018JB015635>
- Schmiedes, J., & Archuleta, R. J. (2008). Near-source ground motion along strike-slip faults: Insights into magnitude saturation of PGV and PGA. *Bulletin of the Seismological Society of America*, 98(5), 2278–2290. <https://doi.org/10.1785/0120070209>
- Semmane, F., Cotton, F., & Campillo, M. (2005). The 2000 Tottori earthquake: A shallow earthquake with no surface rupture and slip properties controlled by depth. *Journal of Geophysical Research*, 110, B03306. <https://doi.org/10.1029/2004JB003194>
- Shahri, S. K., & Baker, J. W. (2013). Final Report of the NGA-West2 Directivity Working Group, Chapter 4Rep., Pacific Earthquake Engineering Research Center, University of California, Berkeley, CA.
- Shahri, S. K., & Baker, J. W. (2014). An efficient algorithm to identify strong-velocity pulses in multicomponent ground motions. *Bulletin of the Seismological Society of America*, 104(5), 2456–2466. <https://doi.org/10.1785/0120130191>
- Shearer, P., Hauksson, E., & Lin, G. Q. (2005). Southern California hypocenter relocation with waveform cross-correlation, Part 2: Results using source-specific station terms and cluster analysis. *Bulletin of the Seismological Society of America*, 95(3), 904–915. <https://doi.org/10.1785/01200401168>
- Shi, Z., & Day, S. M. (2013). Rupture dynamics and ground motion from 3-D rough-fault simulations. *Journal of Geophysical Research-Solid Earth*, 118, 1122–1141. <https://doi.org/10.1002/jgrb.50094>
- Simons, M., Fialko, Y., & Rivera, L. (2002). Coseismic deformation from the 1999 Mw 7.1 Hector Mine, California, earthquake as inferred from InSAR and GPS observations. *Bulletin of the Seismological Society of America*, 92(4), 1390–1402. <https://doi.org/10.1785/0120000933>
- Somerville, P. G. (2003). Magnitude scaling of the near fault rupture directivity pulse. *Physics of the Earth and Planetary Interiors*, 137(1–4), 201–212. [https://doi.org/10.1016/S0031-9201\(03\)00015-3](https://doi.org/10.1016/S0031-9201(03)00015-3)
- Somerville, P. G., Smith, N. F., Graves, R. W., & Abrahamson, N. A. (1997). Modification of empirical strong ground motion attenuation relations to include the amplitude and duration effects of rupture directivity. *Seismological Research Letters*, 68(1), 199–222. <https://doi.org/10.1785/gssr.68.1.199>
- Song, S. G. (2015). The effect of fracture energy on earthquake source correlation statistics. *Bulletin of the Seismological Society of America*, 105(2a), 1042–1048. <https://doi.org/10.1785/0120140207>
- Song, S. G., & Dalguer, L. A. (2017). Synthetic source inversion tests with the full complexity of earthquake source processes, including both supershear rupture and slip reactivation. *Pure and Applied Geophysics*, 174(9), 3393–3418. <https://doi.org/10.1007/s0024-017-1514-1>
- Song, S. G., Dalguer, L. A., & Mai, P. M. (2013). Pseudo-dynamic source modelling with 1-point and 2-point statistics of earthquake source parameters. *Geophysical Journal International*, 196(3), 1770–1786. <https://doi.org/10.1093/gji/ggt479>
- Spudich, P., & Chiou, B. S. J. (2008). Directivity in NGA earthquake ground motions: Analysis using isochrone theory. *Earthquake Spectra*, 24(1), 279–298. <https://doi.org/10.1193/1.2928225>
- Spudich, P., & Chiou, B. S. J. (2013). Final Report of the NGA-West2 Directivity Working Group, Chapter 5Rep., Pacific Earthquake Engineering Research Center, University of California, Berkeley, CA.

- Spudich, P., & Olsen, K. B. (2001). Fault zone amplified waves as a possible seismic hazard along the Calaveras fault in Central California. *Geophysical Research Letters*, 28(13), 2533–2536. <https://doi.org/10.1029/2000GL011902>
- Spudich, P., Rowshandel, B., Shahi, S. K., Baker, J. W., & Chiou, B. S. J. (2014). Comparison of NGA-West2 directivity models. *Earthquake Spectra*, 30(3), 1199–1221. <https://doi.org/10.1193/080313eqs222m>
- Thomas, M. Y., & Bhat, H. S. (2018). Dynamic evolution of off-fault medium during an earthquake: A micromechanics based model. *Geophysical Journal International*, 214(2), 1267–1280. <https://doi.org/10.1093/gji/ggy129>
- Vyas, J. C., Mai, P. M., & Galis, M. (2016). Distance and azimuthal dependence of ground-motion variability for unilateral strike-slip ruptures. *Bulletin of the Seismological Society of America*, 106(4), 1584–1599. <https://doi.org/10.1785/0120150298>
- Vyas, J. C., Mai, P. M., Galis, M., Dunham, E. M., & Imperatori, W. (2018). Mach wave properties in the presence of source and medium heterogeneity. *Geophysical Journal International*, 214(3), 2035–2052. <https://doi.org/10.1093/gji/ggy219>
- Wald, D. J., Heaton, T. H., & Hudnut, K. W. (1996). The slip history of the 1994 Northridge, California, earthquake determined from strong-motion, teleseismic, GPS, and leveling data. *Bulletin of the Seismological Society of America*, 86(1), S49–S70.
- Wang, Y., & Day, S. M. (2017). Seismic source spectral properties of crack-like and pulse-like modes of dynamic rupture. *Journal of Geophysical Research: Solid Earth*, 122, 6657–6684. <https://doi.org/10.1002/2017jb014454>
- Wang, Y., Day, S. M., & Denolle, M. A. (2019). Geometric controls on pulse-like rupture in a dynamic model of the 2015 Gorkha earthquake. *Journal of Geophysical Research: Solid Earth*, 124, 1544–1568. <https://doi.org/10.1029/2018JB016602>
- Withers, K. B., Olsen, K. B., Day, S. M., & Shi, Z. (2018). Ground motion and intraevent variability from 3D deterministic broadband (0–7.5 Hz) simulations along a Nonplanar Strike-Slip Fault. *Bulletin of the Seismological Society of America*, 109(1), 229–250. <https://doi.org/10.1785/0120180006>
- Withers, K. B., Olsen, K. B., Shi, Z., & Day, S. M. (2018). Validation of deterministic broadband ground motion and variability from dynamic rupture simulations of buried thrust earthquakes. *Bulletin of the Seismological Society of America*, 109(1), 212–228. <https://doi.org/10.1785/0120180005>
- Wollherr, S., Gabriel, A. A., & Mai, P. M. (2019). Landers 1992 “reloaded”: Integrative dynamic earthquake rupture modeling. *Journal of Geophysical Research: Solid Earth*, 124, 6666–6702. <https://doi.org/10.1029/2018JB016355>
- Wollherr, S., Gabriel, A. A., & Uphoff, C. (2018). Off-fault plasticity in three-dimensional dynamic rupture simulations using a modal discontinuous Galerkin method on unstructured meshes: Implementation, verification and application. *Geophysical Journal International*, 214(3), 1556–1584. <https://doi.org/10.1093/gji/ggy213>
- Xu, S., Ben-Zion, Y., Ampuero, J.-P., & Lyakhovsky, V. (2015). Dynamic ruptures on a frictional interface with off-fault brittle damage: Feedback mechanisms and effects on slip and near-fault motion. *Pure and Applied Geophysics*, 172(5), 1243–1267. <https://doi.org/10.1007/s0024-014-0923-7>
- Yamashita, T. (2000). Generation of microcracks by dynamic shear rupture and its effects on rupture growth and elastic wave radiation. *Geophysical Journal International*, 143(2), 395–406. <https://doi.org/10.1046/j.1365-246x.2000.01238.x>
- Zheng, G., & Rice, J. R. (1998). Conditions under which velocity-weakening friction allows a self-healing versus a cracklike mode of rupture. *Bulletin of the Seismological Society of America*, 88(6), 1466–1483.
- Zinke, R., Hollingsworth, J., & Dolan, J. F. (2014). Surface slip and off-fault deformation patterns in the 2013 MW 7.7 Balochistan, Pakistan earthquake: Implications for controls on the distribution of near-surface coseismic slip. *Geochemistry, Geophysics, Geosystems*, 15, 5034–5050. <https://doi.org/10.1002/2014GC005538>
- Zoback, M. D., & Byerlee, J. D. (1975). Effect of microcrack dilatancy on permeability of westerly granite. *Journal of Geophysical Research*, 80(5), 752–755. <https://doi.org/10.1029/JB080i005p00752>